Multiscale Analysis of Tropical Cyclone Kinematic Structure from Airborne Doppler Radar Composites

ROBERT ROGERS

NOAA/AOML/Hurricane Research Division, Miami, Florida

SYLVIE LORSOLO

University of Miami/Cooperative Institute for Marine and Atmospheric Studies, Miami, Florida

PAUL REASOR, JOHN GAMACHE, AND FRANK MARKS

NOAA/AOML/Hurricane Research Division, Miami, Florida

(Manuscript received 16 December 2010, in final form 17 May 2011)

ABSTRACT

The multiscale inner-core structure of mature tropical cyclones is presented via the use of composites of airborne Doppler radar analyses. The structure of the axisymmetric vortex and the convective and turbulent-scale properties within this axisymmetric framework are shown to be consistent with many previous studies focusing on individual cases or using different airborne data sources. On the vortex scale, these structures include the primary and secondary circulations, eyewall slope, decay of the tangential wind with height, low-level inflow layer and region of enhanced outflow, radial variation of convective and stratiform reflectivity, eyewall vorticity and divergence fields, and rainband signatures in the radial wind, vertical velocity, vorticity, and divergence composite mean and variance fields. Statistics of convective-scale fields and how they vary as a function of proximity to the radius of maximum wind show that the inner eyewall edge is associated with stronger updrafts and higher reflectivity and vorticity in the mean and have broader distributions for these fields compared with the outer radii. In addition, the reflectivity shows a clear characteristic of stratiform precipitation in the outer radii and the vorticity distribution is much more positively skewed along the inner eyewall than it is in the outer radii. Composites of turbulent kinetic energy (TKE) show large values along the inner eyewall, in the hurricane boundary layer, and in a secondary region located at about 2–3 times the radius of maximum wind. This secondary peak in TKE is also consistent with a peak in divergence and in the variability of vorticity, and they suggest the presence of rainbands at this radial band.

1. Introduction

As has been well documented, improvements in tropical cyclone (TC) intensity forecasts lag advances in track forecasts (e.g., Rogers et al. 2006). The multiscale nature of the processes governing TC intensity and structure is a major reason for this forecasting gap (Marks and Shay 1998). These processes range in scale from environmental-scale [$O(1000$ km$)$] to vortex [$O(10$–100 km$)$], convective [$O(1$ km$)$], turbulent [$O(10$–100 m$)$], and microscales [$O(1$–10 mm$)$]. A better understanding and modeling of these processes, and the upscale and downscale interactions among them, is necessary before significant forecast improvements can be realized. Observations across these scales play an important role in this task, both in improving our understanding of the relevant physical processes and the modeling of them through rigorous data assimilation and detailed model evaluation. A reliable and robust assessment of TC structure across multiple scales is thus an important tool in improving TC intensity and structure forecasts.

A variety of observational platforms have been used to document the structure of tropical cyclones. While satellites have provided vital information primarily on the environment of TCs, aircraft (operating mostly in

Corresponding author address: Robert Rogers, NOAA/AOML Hurricane Research Division, 4301 Rickenbacker Causeway, Miami, FL 33149.
E-mail: robert.rogers@noaa.gov

the Atlantic basin) provide the best observations of the inner-core[1] kinematic and thermodynamic structure of TCs that are outside the range of coastal Doppler radars. Airborne sampling using the National Oceanic and Atmospheric Administration (NOAA) WP-3D aircraft has included flight-level data (e.g., Jorgensen 1984; Jorgensen et al. 1985; Kossin and Eastin 2001; Mallen et al. 2005; Eastin et al. 2005a; Rogers and Uhlhorn 2008), global positioning system (GPS) dropsonde data (e.g., Franklin et al. 1993, 2003; Bell and Montgomery 2008), stepped-frequency microwave radiometer (SFMR; Uhlhorn et al. 2007; Uhlhorn and Black 2003; Rogers and Uhlhorn 2008), and airborne Doppler radar (e.g., Jorgensen 1984; Marks 1985; Marks and Houze 1987; Houze et al. 1992; Marks et al. 1992; Gamache et al. 1993; Franklin et al. 1993; Dodge et al. 1999; Reasor et al. 2000, 2005, 2009; Marks et al. 2008; Lorsolo et al. 2010). A summary of research conducted over 30 years using the NOAA WP-3D aircraft can be found in Aberson et al. (2006a).

From these studies and others, a general depiction of TC structure has been obtained. For example, the symmetric primary circulation is characterized by a tangential wind maximum that slopes outward with height, while the secondary circulation has a deep (surface to ~5-km altitude) layer of radial inflow in the lower troposphere, a layer of intense outflow above 10-km altitude, and a rising branch collocated with the eyewall and sloping radially outward with height (e.g., Marks and Houze 1987; Houze et al. 1992; Marks et al. 1992; Gamache et al. 1993). In terms of asymmetric structures, low azimuthal wavenumber asymmetric structures such as shear-induced vortex tilt and asymmetries in wind and rainfall (Marks et al. 1992; Reasor et al. 2000, 2009; Black et al. 2002), high-wavenumber asymmetries such as vortex Rossby waves and eyewall mesovortices and misovortices (Aberson et al. 2006b; Montgomery et al. 2006a; Marks et al. 2008), and low-level kinematic and thermodynamic structures in the inner core, including rainband regions (Barnes et al. 1983; Powell 1990; Barnes and Powell 1995; Cione et al. 2000) have all been documented. In addition to describing these vortex-scale structures, various observational studies have looked at statistical properties of convective-scale vertical velocity, mass flux, and reflectivity (Jorgensen 1984; Jorgensen et al. 1985; Black et al. 1996; Eastin et al. 2005a; Rogers et al. 2007; Hence and Houze 2008; Didlake and Houze 2009; Houze

et al. 2009; Braun et al. 2010), and turbulent-scale kinetic energy (Lorsolo et al. 2010), including how they vary for different regions and periods within a TC life cycle.

Many of these studies have involved examinations of individual cases. While this approach can yield detailed information on the case being considered, they are by definition limited in their ability to be applied to a broad range of environments and TC structures. Composites can be helpful for applying these conclusions to a broad set of situations, enabling analyses where observations from an individual case may be insufficient. Such composite studies have revealed important characteristics about TC structure and evolution using a variety of datasets. For example, by compositing flight level, Shea and Gray (1973) and Gray and Shea (1973) found that the inflow is confined to the lowest layers outside the radius of maximum wind, outflow occurs aloft inside the radius of maximum wind, and the largest convergence occurs in the lowest levels beneath the radius of maximum wind. Also compositing flight-level data, Kossin and Eastin (2001) found two distinct regimes distinguished by the radial gradient of tangential wind and vertical vorticity. They attributed each regime to storms that are either intensifying or have reached peak intensity. Eastin et al. (2005a) composited flight-level data to document statistics of vertical motion in the inner core of intense hurricanes, finding that the upward motion in the eyewall comprises a combination of intense convective cores superposed on symmetric, near-moist-neutral ascent. Using composites of GPS dropsondes, Franklin et al. (2003) documented the mean vertical profile of wind speed in the hurricane inner core from the surface to 700 hPa, finding that, on average, the surface wind is about 90% of the 700-hPa value. Frank (1982) composited rawinsonde data from the Caribbean Sea and west Pacific to find that the radial wind and vertical motion anomalies associated with the genesis and intensification of tropical cyclones are confined to the inner 6° and 2° from the TC center, respectively, while the tangential circulation increases to at least the 15° radius.

Composites of airborne Doppler radar data, collected by the NOAA Hurricane Research Division (HRD) for the past 30 years, provide information on three-dimensional TC inner-core kinematic structures in a statistically robust framework. The ability to construct composites of airborne Doppler radar data has been facilitated by the development of an automated processing algorithm based on a variational scheme first described in Gamache (1997) and documented in detail in Reasor et al. (2009). Stern and Nolan (2009) used these automated analyses to examine the vertical structure of axisymmetric tangential wind in individual analyses from multiple radial aircraft penetrations, but

---

[1] For the purpose of this study, "inner core" is defined as all radii within 4 times the radius of maximum wind. Since the airborne Doppler gridded analyses are 400 km on a side, the inner core is included in the analyses (subject to the availability of scatterers, beam spreading, and attenuation).

TABLE 1. List of storms used in Doppler composite. Best-track intensity of storm at the time of radar analyses, 24-h change in intensity centered at the analysis times, and radius of maximum axisymmetric tangential wind at 2-km altitude included.

Storm name	Date	No. of radial penetrations	Best-track intensity (m s^{-1})	24-h intensity change (m s^{-1})	Radius of peak axisymmetric wind at 2-km altitude (km)
Guillermo	2 Aug 1997	4	57	27	33
Fabian	3 Sep 2003	3	59	−3	25
Isabel	12 Sep 2003	2	76	−5	35
Isabel	13 Sep 2003	1	76	3	44
Isabel	14 Sep 2003	4	76	−5	49
Frances	30 Aug 2004	3	59	8	41
Frances	31 Aug 2004	2	68	3	35
Frances	1 Sep 2004	3	65	3	38
Ivan	7 Sep 2004	4	57	14	18
Katrina	28 Aug 2005	1	81	0	30
Katrina	29 Aug 2005	3	59	−49	57
Rita	21 Sep 2005	3	78	24	26
Rita	22 Sep 2005	3	68	−22	21
Paloma	8 Nov 2008	4	68	−30	17

they did not composite them on the assumption that size and structure variations would obscure a meaningful signal. The work presented in this manuscript is the first time an effort has been undertaken to construct composites of TC inner-core structure from multiple TCs using airborne Doppler radar data. As will be shown here, compositing Doppler analyses by accounting for variations in the TC size preserves a robust signal that agrees well with many previous case studies and composites using other observational datasets and also combines the advantages of using three-dimensional Doppler radar observations with the advantages inherent in the compositing technique. Multiple applications are also possible using this compositing methodology that complement well the case-study approach. The purpose of this work is to present these composites and document how they compare with past studies, with an emphasis on how the composites depict structures across multiple scales (i.e., vortex, convective, and turbulent scale). Such an approach can be used to better understand physical processes important in TC intensity change and to evaluate numerical models.

2. Methodology

a. Dataset

Composites of inner-core structure are created using tail Doppler radar data from NOAA WP-3D radial penetrations in multiple storms from 1997 to 2008. A total of 40 radial penetrations from 14 flights in 8 different tropical cyclones, all of hurricane intensity, during this time period are included in the composites (Table 1). The hurricanes that were included, along with some noteworthy studies about them, are Guillermo (1997) (Eastin

et al. 2005b; Reasor et al. 2009; Sitkowski and Barnes 2009), Fabian (2003) (Drennan et al. 2007; Black et al. 2007), Isabel (2003) (Aberson et al. 2006b; Montgomery et al. 2006a; Drennan et al. 2007; Bell and Montgomery 2008), Frances (2004) (Black et al. 2007; Lorsolo et al. 2008), Ivan (2004) (Eastin and Link 2009; Baker et al. 2009), Katrina (2005) (Houze et al. 2006; McTaggart-Cowan et al. 2007; Houze et al. 2007; Squires and Businger 2008; Hence and Houze 2008; Didlake and Houze 2009), Rita (2005) (Houze et al. 2007; Hence and Houze 2008; Squires and Businger 2008), and Paloma (2008). Figure 1 shows reflectivity from the WP-3D lower-fuselage radar for each flight used in the composites. All of the hurricanes were of at least category 3 intensity on the Saffir–Simpson scale (52 m s^{-1} or greater) at the time of the analyses, according to the best track. Several hurricanes, including Hurricanes Isabel, Katrina, and Rita, were category 5 at the time of the sampling. The reflectivity patterns shown in Fig. 1 clearly show the eyewall in each case and the case-to-case variability of the radius of the eyewall. The hurricanes with the smallest eyewall radius (Table 1, Fig. 1) were Ivan (7 September 2004), Rita (22 September 2005), and Paloma (8 November 2008), while the storms with the largest eyewall radius were Isabel (13–14 September 2003) and Katrina (29 August 2005). Many of the cases showed rainbands spiraling outward from the center to several times the eyewall radius [e.g., Fabian (3 September 2003), Frances (30 August 2004), Ivan (7 September 2004), Paloma (8 November 2008)], while some cases also exhibited concentric eyewalls roughly 2–3 times the radius of the inner eyewall [e.g., Isabel (12 September 2003), Katrina (28 August 2005), Rita (22 September 2005)]. Some cases showed a symmetric eyewall reflectivity pattern
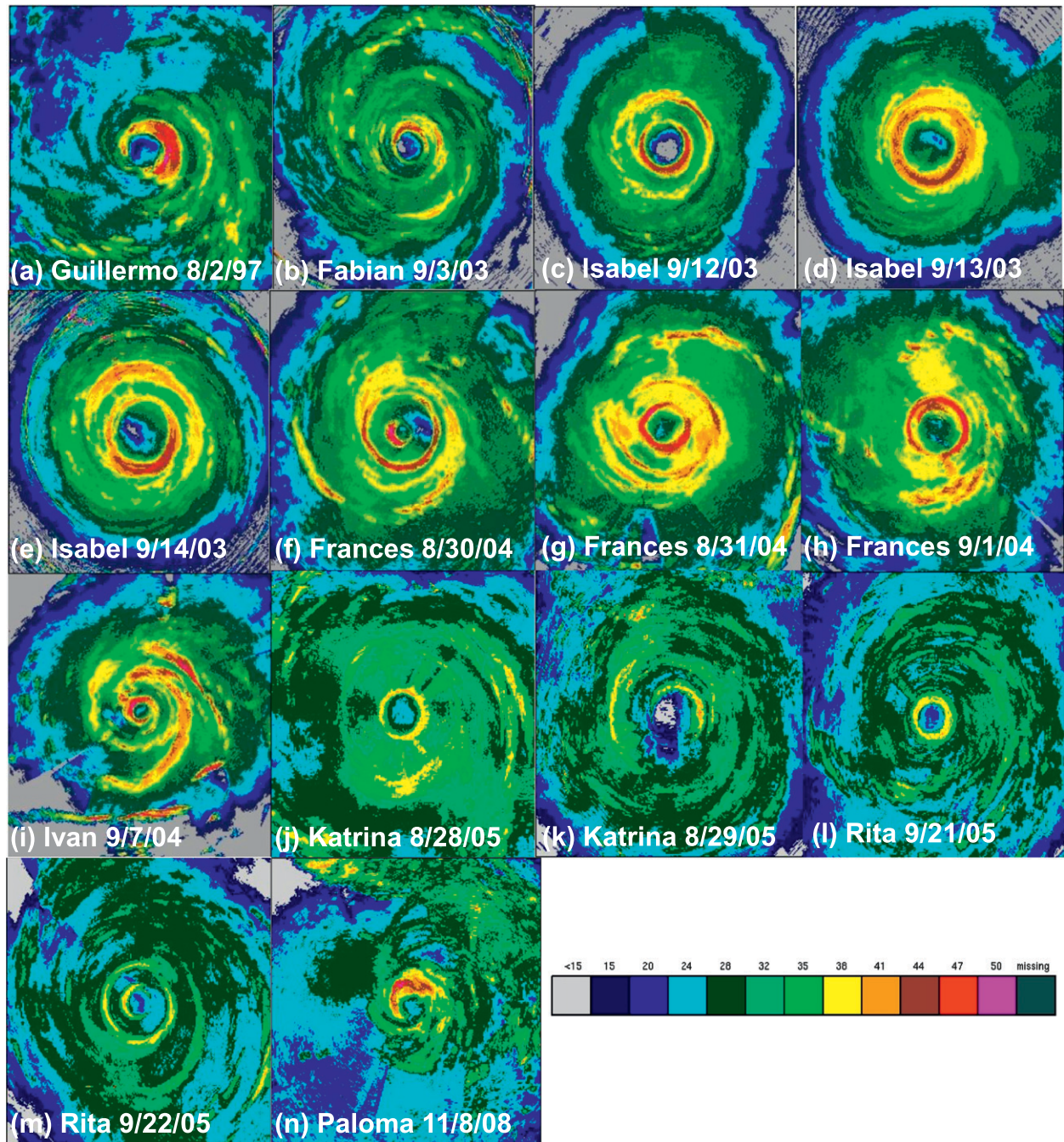
MONTHLY WEATHER REVIEW

FIG. 1. Lower-fuselage composites of reflectivity (shaded, dBZ) from each flight for the Doppler analyses used to construct Doppler composites. (a) Guillermo, 1915–1945 UTC 2 Aug 1997; (b) Fabian, 1929–1949 UTC 3 Sep 2003; (c) Isabel, 1842–1907 UTC 12 Sep 2003; (d) Isabel, 1830–1900 UTC 13 Sep 2003; (e) Isabel, 1822–1852 UTC 14 Sep 2003; (f) Frances, 1923–1943 UTC 30 Aug 2004; (g) Frances, 1711–1731 UTC 31 Aug 2004; (h) Frances, 1658–1718 UTC 1 Sep 2004; (i) Ivan, 1920–1940 UTC 7 Sep 2004; (j) Katrina, 2020–2100 UTC 28 Aug 2005; (k) Katrina, 0900–0940 UTC 29 Aug 2005; (l) Rita, 1545–1620 UTC 21 Sep 2005; (m) Rita, 1850–1940 UTC 22 Sep 2005; and (n) Paloma, 1825–1905 UTC 8 Nov 2008. All images are 360 km on a side. Aircraft altitude for all composites is between 1.5 and 3.5 km.

[e.g., Isabel (13 September 2003) and Frances (31 August 2004)], while other cases showed a more asymmetric reflectivity pattern [e.g., Guillermo (2 August 1997) and Fabian (3 September 2003)]. The storms exhibited a range of intensity changes, with 1 storm intensifying by 27 m s^{-1} (Guillermo) and another weakening by 30 m s^{-1} (Paloma, due to strong shear and landfall in Cuba) during the 24 h centered on the radar leg. More

than half of the storms experienced a 24-h intensity change of <10 m s^{-1} during the time of the radar leg, however.

b. Data processing methodology

An automated variational algorithm (Gamache 1997) of reflectivity and Doppler radial velocity is used here. The analyses produced are a global three-dimensional variational solution of the continuity and Doppler projection equations, similar to that done in Gao et al. (1999) and Reasor et al. (2009) and used in Stern and Nolan (2009). The analyses are obtained from radial legs flown by the NOAA WP-3D aircraft. The length of each radial leg (end point to storm center) ranges from ~120 to 180 km, so the total along-track distance for each leg is ~240–360 km. Two primary analyses are generated for each radial pass: a three-dimensional Cartesian grid (called a swath here) and a two-dimensional profile of horizontal and vertical winds and reflectivity oriented parallel to the aircraft flight track. The swath analyses have a horizontal grid spacing of 2 × 2 km^2 and a vertical spacing of 0.5 km. The domain size of the swath analyses is 400 × 400 km^2, though the areal coverage of data is generally much less than this because of the availability of scatterers and attenuation. The profile analyses are calculated by incorporating data above and below the aircraft in a 10-km-wide region normal to the aircraft track (Lorsolo et al. 2010). The same precipitation terminal fall speed is used in both methods; however, the fall speed is removed before interpolating the Doppler radials observations to produce the swath solution, while the results of the profile solution are the three components of precipitation motion, the vertical wind being obtained by subtracting the fall speed. The resulting profile analysis is a two-dimensional field of winds and reflectivity, with an along-track spacing of 1.5 km and a vertical spacing of 0.15 km. Figure 2 shows an example of both analysis products from Hurricane Guillermo (1997), including a vertical cross section of wind speed taken along the aircraft track from both the swath and profile analyses. The resolution differences between the swath and profile analyses largely explain the differences seen in the cross sections of wind speed in Figs. 2b,c, in particular the finer vertical structure seen in the profile analysis.

To calculate several parameters related to the symmetric structure of the storm composites, the Cartesian data from the swaths are interpolated to cylindrical coordinates. The storm center is defined using a simplex algorithm (Neldar and Mead 1965) that maximizes tangential wind in a 5-km-wide annular ring centered on the radius of maximum wind. The center location thus varies in height, and the azimuthal mean fields at each height
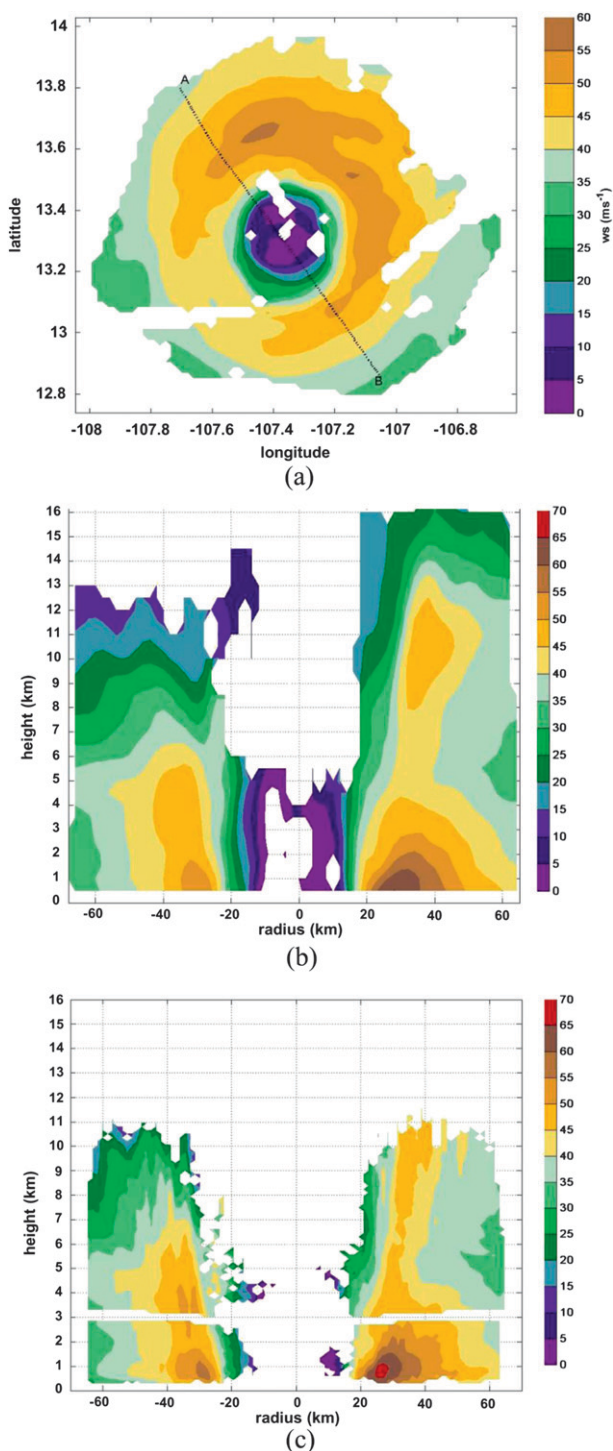

(a)

(b)

(c)

FIG. 2. Example of radar analyses used in composites. (a) Wind speed (m s^{-1}) at 3-km altitude for 2 Aug 1997 from Hurricane Guillermo. (b),(c) Line AB in (a) denotes location of cross sections of wind speed. (b) Cross section of wind speed (m s^{-1}) produced from swath analysis. (c) As in (b), but for profile analysis.
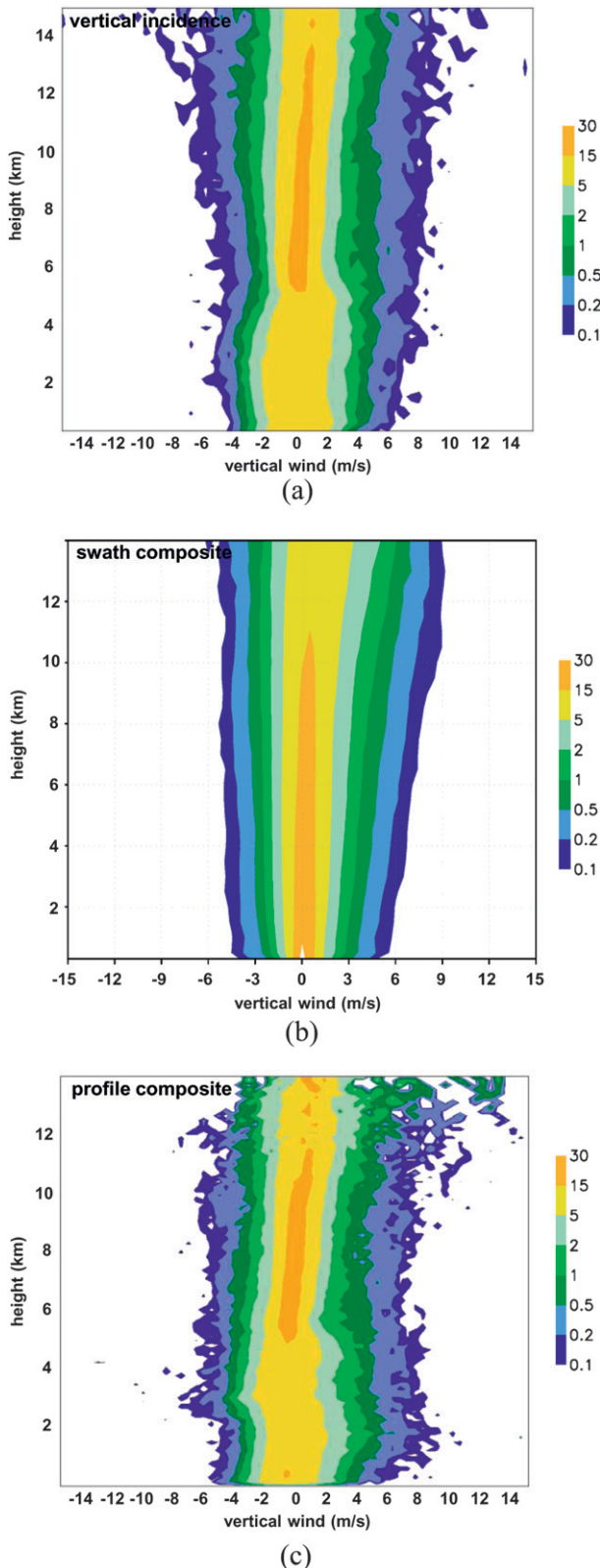
FIG. 3. CFADs of vertical velocity (shaded, %) from entire radial domain for (a) vertical incidence dataset from Black et al. (1996), (b) swath data, and (c) profile data.

shown here are calculated relative to the center at that height. This algorithm is similar to what has been done in previous airborne and ground-based radar and numerical modeling studies of TCs (e.g., Marks et al. 1992; Lee and Marks 2000; Reasor et al. 2000; Rogers et al. 2003). Since different storms are of different sizes, it is necessary to map the radial legs onto a normalized coordinate system in order to perform the composites. This is done by calculating a normalized radius and plotting all relevant fields as a function of this normalized radius. The normalized radius $r*$ is defined by $r* = r/\mathrm{RMW}_{2km}$, where r is the radial distance from the center and RMW_{2km} is the radius of maximum axisymmetric tangential wind at 2-km altitude, an altitude consistent with that used in Stern and Nolan (2009).

c. Comparison of swath and profile composites

There are several differences in the swath and profile analyses that arise from the characteristics of the analysis grid as well as the way various calculations are handled. Some of these differences are seen in the example shown in Fig. 2. For example, a key difference between the two analyses is that the profiles produce analyses closer to the surface (i.e., 150 m) compared with the minimum altitude of 500 m from the swath data. This proximity to the surface allows the profile composite to capture a significant component of the low-level inflow compared with the swath composite (shown later). While the profiles can better depict the boundary layer, the swath analyses are preferred for higher altitudes, because the profile analyses only extend to ~10-km altitude before data coverage limitations within the 10-km-wide averaging distance preclude sufficient sampling of the tangential wind component. For this reason the swath analyses better represent the outflow-layer structure. Finally, as can be seen in Fig. 2, there are often more data inside the radius of maximum wind (RMW) for the swath compared to the profile analyses.

Vertical velocity analyses can also differ significantly. These differences are attributable to two primary factors: the greater azimuthal coverage by the swaths, which can be significant for a field like vertical velocity that can show significant azimuthal variability, and the different way that vertical velocity is calculated for the swaths and the profiles. The swath analyses estimate winds in all three dimensions by solving the continuity and Doppler-projection equations simultaneously and globally, after subtracting the component of the estimated fall speed of the hydrometeors along the Doppler radial. The profile analyses estimate vertical velocity solely by subtracting the estimated fall speed from the overdetermined precipitation-motion solution (i.e., with no need for applying a continuity constraint). For this reason, the vertical

velocity from the profile data has typically been considered a more reliable solution (Marks and Houze 1987), though both methods of calculation are considered here. To ensure the features at a particular altitude were consistently resolved, a constant 10-km strip is used in the cross-track direction. Vertical wind errors in the profiles are increased near the flight level due to the Doppler sampling of primarily horizontal wind in this area. In the same way, tangential wind estimates in the profiles will be best near flight-level and degrade at altitudes higher than the aircraft. Radial-wind estimate errors should not vary significantly with height, since all measurements at all levels project approximately 20° in the radial direction (neglecting drift angle).

Despite the differences in the analyzed fields from the swaths and profiles described above, statistics of vertical velocity are generally consistent between them. Contoured frequency by altitude diagrams (CFADs; Yuter and Houze 1995) of vertical velocity from the swath and profile composites for the entire radial domain (Fig. 3) show that, in general, both datasets have the bulk of their vertical velocities between -2 and 2 m s^{-1}, with small percentages of the up- and downdrafts as large as 6–8 m s^{-1}. The most notable differences between the two datasets are a broader distribution in the lowest 4 km and slightly stronger peaks in the profile data. It is expected that the profile method, with higher resolution, and no continuity solution, can better resolve these peaks. Modal values of vertical velocity are comparable between the swaths and the profiles, but the values of the extreme portions of the distribution (top and bottom 0.2%) can be up to 50% larger in the profiles.[2] The CFADs from this dataset, in particular from the profiles, are also similar to the CFAD calculated from the vertical incidence database from Black et al. (1996), as shown in Fig. 3a. Most of the minor differences seen between the profile and VI CFADs are believed to be due to the biases mentioned in the footnote, so at this time the vertical incidence CFAD of vertical velocity appears to be the most reliable.

In summary, both the swath and profile composites have their advantages. The swath analyses produce three-dimensional fields of horizontal and vertical wind and reflectivity that better represent the axisymmetric structure, and they extend to a higher altitude and include more data inside the RMW than do the profile analyses. However, vertical resolution is limited, they are limited in how close to the surface they can reliably measure the winds, and there is an additional uncertainty in the vertical velocity calculation that arises from the use of the continuity constraint, but they also have uncertainty resulting from the subtraction of a terminal fall speed. The profile analyses have better vertical and radial resolution and do not have this continuity constraint. As a result they better resolve the low-level inflow and produce more detail in all three wind components, especially outside of the eyewall. However, the azimuthal coverage is limited and three-dimensional spatial coverage is not possible. Furthermore, quantities requiring derivatives in the azimuthal direction cannot be computed from the profiles, with the exception of azimuthal-mean vertical vorticity and horizontal divergence, which could be estimated from inbound–outbound profile averages. For this paper, both the swath and profile analyses will be considered for the tangential, radial, and vertical wind analyses in order to take advantage of the benefits of each analysis methodology. For the absolute angular momentum field, only the profile analysis will be shown, while for the reflectivity, vorticity, and divergence fields, only the swath analyses will be shown. For the convective-scale statistics, the swath analyses are used because of their greater spatial coverage and resulting increased sample size, while for the turbulent-scale properties only the profile analyses are used.

d. Error statistics

Because all the data included in this study were produced with an algorithm using automatic editing and quality control, it is important to assess the accuracy and quality of data stemming from this type of processing. Reasor et al. (2009) provided a detailed evaluation of the three-dimensional variational analysis used in the processing and showed that the derived winds were of good quality using manual editing. The present study uses automated editing, thus it is necessary to evaluate the accuracy of the technique.

Root-mean-squared (RMS) error, bias and linear correlation coefficients were computed for comparison with flight-level data for tangential V_t, radial V_r, and vertical w winds from both automated (including swath and profile analyses) and manual editing. All radar analyses from Hurricane Guillermo (1997) were compared to flight-level data, with the comparison between the manually edited data and the flight-level data being considered the reference. The comparison was obtained by first filtering the flight-level data to match the radar resolution. The radar analyses were then interpolated to the

---

[2] Some of the differences between the swath and the profile vertical velocities are due to a bias that has been noted in the profile vertical velocity calculation, in particular an above (below) flight track negative (positive) bias. Extensive testing has been performed to attempt to isolate the source of this bias, including errors in the radar antenna angles and aircraft attitude. This work is ongoing. The magnitude of the error appears to be no more than ~ 0.5 m s^{-1}, and it does not impact the structure of the dominant signal (i.e., the eyewall updraft).

TABLE 2. (a) Comparison of RMS error, bias, and correlation coefficient between radar-derived and flight-level parameters for Hurricane Guillermo on 2 Aug 1997 using swath data produced using automated algorithm (regular), swath data produced using manual algorithm as in Reasor et al. (2009, italic), and profile data produced using automated algorithm (boldface). (b) As in (a), but for automated swath and profile analyses using all cases shown in Table 1.

(a) Guillermo

	RMS (m s^{-1})	Bias (m s^{-1})	Correlation coef
Vt	2.4/*2.62*/**1.56**	−0.08/*−0.47*/**−0.04**	0.98/*0.95*/**0.98**
Vr	2.73/*2.57*/**3.35**	−1.12/*−1.18*/**−1.6**	0.93/*0.94*/**0.69**
w	1.56/*1.57*/**1.67**	−0.13/*−0.19*/**−0.79**	0.46/*0.51*/**0.39**

(b) All cases

	RMS (m s^{-1})	Bias (m s^{-1})	Correlation coef
Vt	3.72/**2.76**	−0.4/**−0.24**	0.97/**0.98**
Vr	4.6/**3.6**	−0.14/**−0.64**	0.74/**0.76**
w	1.62/**1.41**	0.07/**−0.2**	0.34/**0.30**

flight-level data location using a three-dimensional linear interpolation.

The Hurricane Guillermo analyses from the automated processing perform comparably against the flight-level data compared with the manually edited analyses for the tangential, radial, and vertical wind (Table 2a). These results confirm that the automated processing produced wind analyses of a quality on par with the processing using manually edited data. The entire dataset was then compared to flight-level data (Table 2b) and shows comparable results between swath and profile analyses. Figures 4–6 illustrate this result, exhibiting overall similar distributions between flight-level data and the swath and profile analyses.

e. Analysis strategy

The primary parameters analyzed here span the vortex- to the turbulent scale. Vortex-scale fields include the axisymmetric fields of tangential, radial, and vertical wind, reflectivity, vertical vorticity, and divergence. For the calculations of the axisymmetric fields, data at a particular radius are only included in the compositing if the maximum azimuthal gap is less than 180°. Convective-scale fields are assessed by examining the statistical properties of vertical velocity and vertical vorticity at each grid point (2 km × 2 km × 0.5 km) in the swath analyses, and how those statistics vary as a function of proximity to RMW_{2km}. Turbulent-scale fields are evaluated using a composite of turbulent kinetic energy from the profile analyses (1.5 km × 0.15 km), in a manner similar to that done in Lorsolo et al. (2010), and examining how it varies as a function of normalized radius. Composites of asymmetric structures, including detailed comparisons of vortex tilt, are the subject of future work.
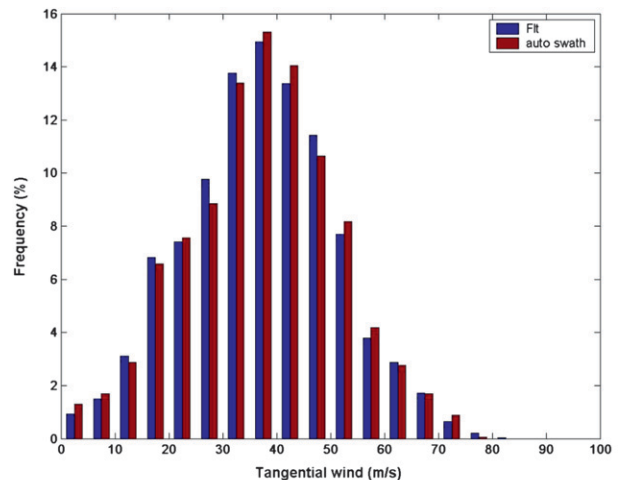

(a)
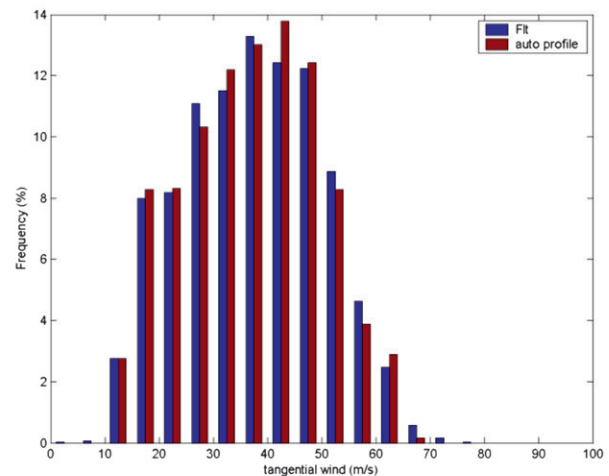
(b)

FIG. 4. Histogram comparing the distribution of tangential wind from all radar legs from (a) flight-level data and swath analyses, and (b) flight-level data and profile analyses.

3. Results

a. Axisymmetric eyewall characteristics

Summary statistics of eyewall characteristics from the 40 radar legs are shown in Table 3. The average eyewall radius, assumed here to correspond to the radius of the maximum axisymmetric wind at 2-km altitude (RMW_{2km}), is 32.6 km, with a minimum of 14 km and a maximum of 66 km. Given that the length of the radial penetrations is ∼120–180 km (see above), information out to $r* = 2$–3 is available for most cases. However, information beyond $r* = 3$ is more limited, particularly for cases with large RMW_{2km} (e.g., Katrina on 29 August
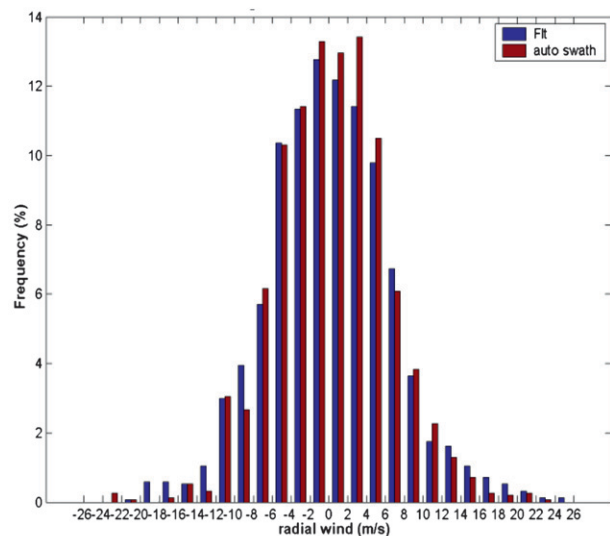
(a)
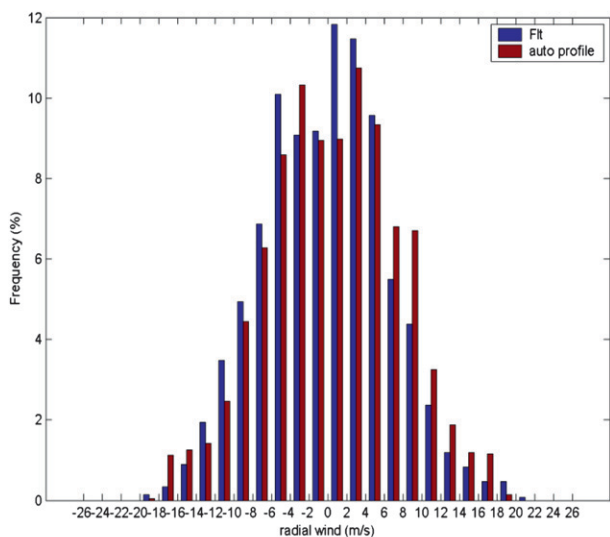
(b)

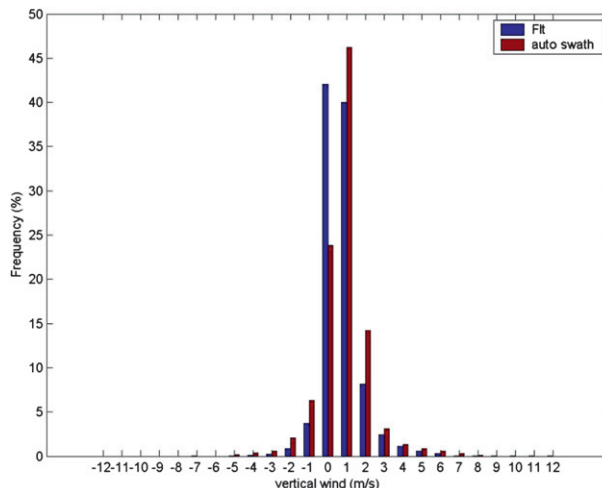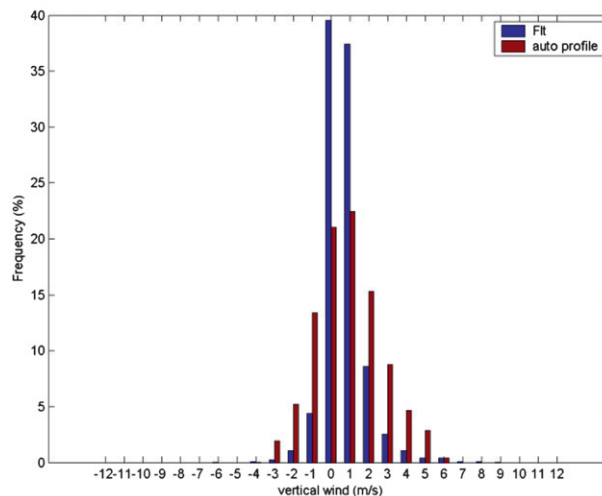FIG. 5. As in Fig. 4, but for radial wind.

(a)

(b)

FIG. 6. As in Fig. 4, but for vertical wind.

2005, cf. Table 1). This may indicate that smaller storms are more represented in the composite analysis at these larger radii. The RMW slope, defined as the difference between the radius of peak axisymmetric wind at 2- and 8-km altitude [similar to that done in Stern and Nolan (2009)] varies between a ratio of −0.67 and 1.67, with a mean value of 0.63 and a standard deviation of 0.57. This translates to a slope ranging between −33° and 59°, with a mean of 28° and a standard deviation of 24°. This range of values compares well with that found in Stern and Nolan (2009), who found an average slope of 32° and a standard deviation of 26° for the cases they examined (calculated from their Table 1).

b. Axisymmetric structure of vortex-scale fields

Figure 7 shows normalized radius–height ($r*$–z) plots of axisymmetric tangential and radial wind fields obtained by compositing the swath and profile analyses. To ensure that an adequate number of analyses compose the composite, the only areas shown in $r*$–z space are where data from at least 50% of the analyses are present. Many features of the primary and secondary circulation commonly seen in individual case studies (Marks and Houze 1987; Marks et al. 1992) are seen in the composites. Tangential wind in the swath composite is maximized at $r* = 1$ with a peak value of 60 m s^{-1} at 1-km altitude, decreasing to 40–45 m s^{-1} by $r* = 2$ and to 35 m s^{-1} by $r* = 3$. The eyewall slope (in the mean) is also seen in this composite, as the radius of peak

TABLE 3. Summary statistics of eyewall characteristics from all 40 radar legs.

	Min	Max	Mean	Std dev
RMW_{2km} (km)	14	66	32.6	12.7
2–8-km slope of RMW (ratio)	−0.67	1.67	0.63	0.57
2–8-km slope of RMW (°)	−33.7	59	27.90	24.10

axisymmetric wind increases from $r* = 1$ at 2-km altitude to $r* \sim 1.1$ at 6-km altitude and $r* \sim 1.3$ at 10-km altitude. The value of the peak axisymmetric tangential wind at 2-km altitude is 58 and 46 m s^{-1} at 8 km, or 79% of the value at 2 km. This decay is comparable to the 75%–85% range found in Stern and Nolan (2009). A similar profile is seen in the tangential wind composite from the profiles, including the peak wind near 1-km altitude at $r* \sim 1$ and the sloping eyewall. There is an indication of a slower radial decay of tangential wind below 5-km altitude outside the eyewall compared with the swath composite.

The axisymmetric radial flow from the swath composite (Fig. 7c) shows the lower-tropospheric inflow reaching a peak value of −4 m s^{-1} at 0.5-km altitude. A region of enhanced low-level outflow is also seen just inside the RMW between 1 and 3 km. Outflow associated with the sloping eyewall is also apparent, as is the strong outflow associated with the outflow layer above 12 km. A secondary region of outward motion is apparent beyond $r* = 2.5$ in the 6–10-km layer. With its higher vertical resolution and ability to extend closer to the surface, the radial flow from the profiles clearly shows strong low-level inflow of −15 m s^{-1} below 0.5 km. The depth of the inflow layer varies from about 1- to 1.5-km altitude between $r* = 1$ and 2.5. The low-level outflow inside the RMW is much better depicted in the profile composite, with a peak outflow value >3 m s^{-1}. The outflow region beyond $r* = 2.5$ in the 6–10-km layer is also apparent in the profile composite.

The axisymmetric vertical velocity from the swath composite (Fig. 7e) shows the eyewall updraft located radially inward of the tangential wind peak (cf. Fig. 7a) and extending from the boundary layer to 14-km altitude, reaching a peak near 2.5 m s^{-1} at 12 km. Some error in this velocity may result from the insufficient resolution of boundary layer inflow, but it is mitigated somewhat by the inclusion of many Doppler radial observations pointing nearly vertically near the flight track and the use of weak boundary conditions. Just outside the eyewall the upward motion decreases sharply, dropping to near 0 m s^{-1} at $r* = 1.3–1.5$. Radially outward an area of upward motion from $r* = 2–2.5$ is located above 6-km altitude, coincident with the area of enhanced outflow from the radial wind composite (cf. Figs. 7c,d). The profile composite of

axisymmetric vertical velocity shows many similar features as the swath composite, but the peak eyewall updraft is at two altitudes: one near 1.5-km altitude coincident with the outflow shown in the radial composite and the other at 4–5 km. The broad updraft maximum is also seen at $r* = 2–3$, similar to that seen in the swath composite. The profile composite also captures an area of pronounced downward motion just outside the eyewall, extending from 2–8-km height, which is not seen in the swaths. The profile composite also shows an area of weak ascent below 3-km altitude in the $r* = 2–3$ band, in contrast with the expected region of weak subsidence associated with stratiform precipitation in the outer radii (e.g., Marks and Houze 1987). Possible explanations for this discrepancy include the presence of secondary eyewalls in some of the radar legs and the errors in profile-derived vertical velocity mentioned in section 2c.

The composite absolute angular momentum and secondary circulation vectors from the profile composite are shown in Fig. 8a. The secondary circulation vectors show that the eyewall updraft does ascend along the angular momentum surface, similar to that described by Emanuel (1986). There is an indication of flow crossing the angular momentum surface at the 1-km altitude in the inflow layer. This crossing is even more pronounced below 1-km altitude, where the strong low-level inflow is clearly seen. The secondary circulation also crosses angular momentum surfaces up to $\sim$5 km, but the inflow is weaker at these altitudes. Such slow inflow can spin up the vortex without the offsetting effects of friction. This is consistent with observations presented in Eastin et al. (2005b) and Ooyama's conceptual model of axisymmetric hurricane evolution (Ooyama 1982).

A plot of the symmetric reflectivity from the swath composite (Fig. 8b) shows the highest reflectivity below 3-km altitude located just inside $r* = 1$ (i.e., along the inner edge of the eyewall). This peak reflectivity extends upward just inside the radius of peak tangential wind and just outside the vertical wind peak (cf. Fig. 7). The relative radial location of the reflectivity and vertical velocity maxima is consistent with individual cross sections of vertical incidence data in Black et al. (1996). Outside the eyewall the reflectivity is characteristic of predominantly stratiform precipitation, with a broad horizontal distribution extending out to $r* = 3$ and a sharp vertical gradient just above the melting level (i.e., $\sim$5-km altitude). This general pattern of a deep layer of reflectivity in the eyewall and a broad area of stratiform-type reflectivity radially outward has been documented in Marks and Houze (1987). An area of slightly higher reflectivity at 1–2-km altitude is located between $r* = 2$ and 3, at a radius coincident with the upper-level outflow and weak upward motion shown in Fig. 7.
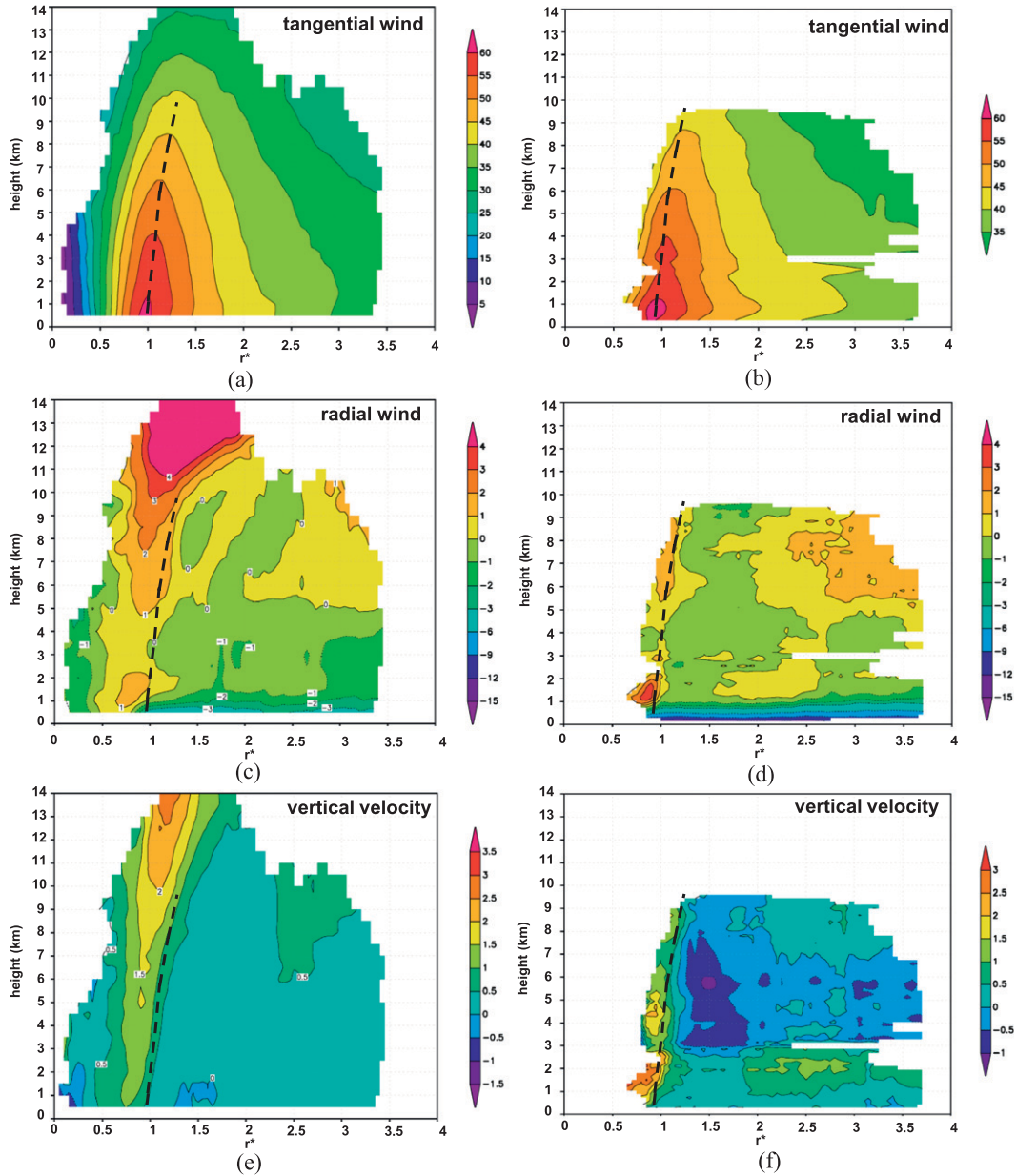
FIG. 7. (a) Composite axisymmetric tangential wind (m s^{-1}) from swath data. (b) Composite axisymmetric tangential wind (m s^{-1}) from profile data. (c) As in (a), but for radial wind (m s^{-1}). (d) As in (b), but for radial wind (m s^{-1}). (e) As in (a), but for vertical wind (m s^{-1}). (f) As in (b), but for vertical wind (m s^{-1}). All composites calculated using radar legs from Table 1, plotted as a function of normalized radius $r*$ and height AGL. Data from a minimum of 20 analyses are required for plotting. The dashed line denotes the axis of peak axisymmetric tangential wind from 0.5- to 10-km altitude calculated from the swath composite in (a).

The vorticity (Fig. 8c) shows maximum axisymmetric vorticity values of 50×10^{-4} s^{-1} along the inner edge of the eyewall, near $r* = 0.75$ and below 1-km altitude. The axis of peak vorticity is located inside the RMW and slopes outward with increasing altitude, consistent with the eyewall slope shown in Fig. 7 and Table 3. Radially inward of the peak vorticity the values decrease significantly, falling

to $<30 \times 10^{-4}$ s^{-1} at $r* = 0.3$ and 1-km altitude. Such a radial distribution indicates that, in the mean at least, a ring of vorticity exists for storms from this dataset. Outside the vorticity peak the values rapidly decrease, reaching $\sim7 \times 10^{-4}$ s^{-1} at 1-km altitude, or $\sim25\%$ of their value at the RMW, by $r* = 1.5$. This decrease is generally consistent with that shown in flight-level composites in Mallen et al.
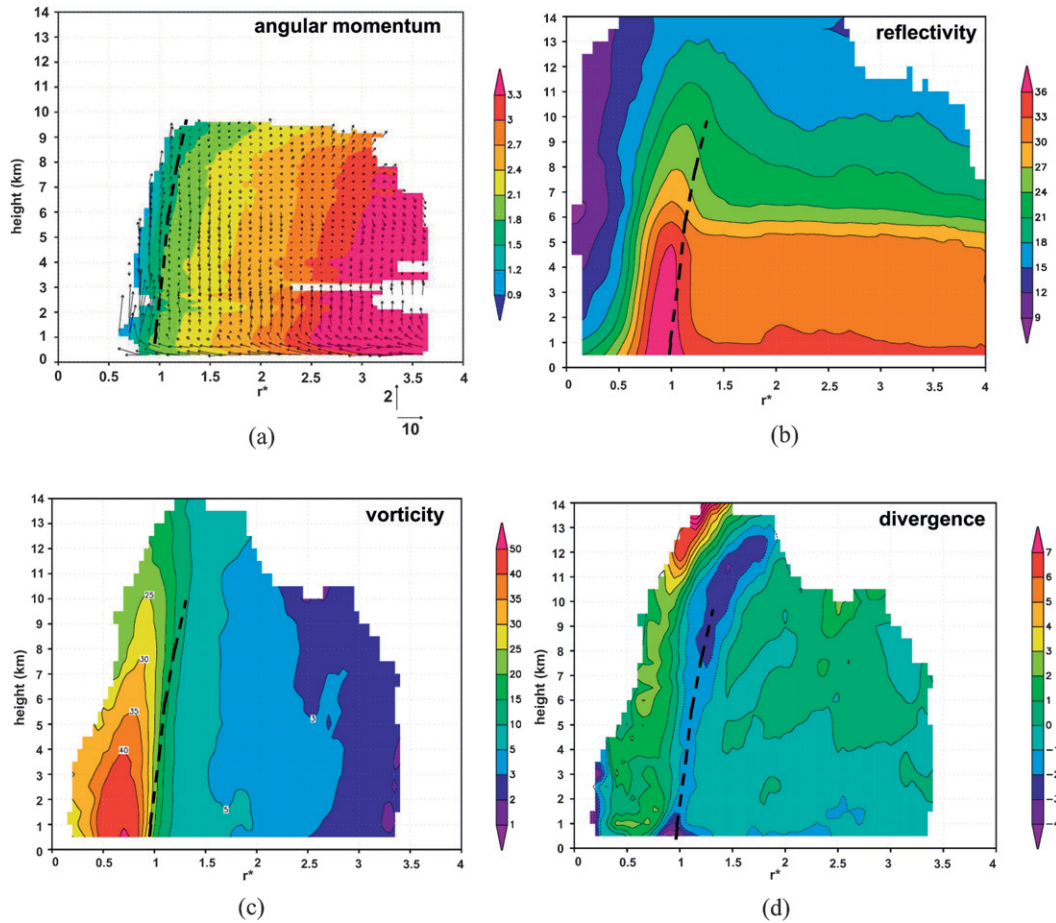
FIG. 8. (a) Composite absolute angular momentum ($\times 10^6$ m^2 s^{-1}) from profile data. (b) Composite axisymmetric reflectivity (dBZ) from swath data. (c) As in (b), but for relative vorticity ($\times 10^{-4}$ s^{-1}). (d) As in (b), but for horizontal divergence ($\times 10^{-4}$ s^{-1}). The dashed line denotes axis of peak axisymmetric tangential wind from 0.5- to 10-km altitude calculated from the swath composite in Fig. 7a.

(2005). An axis of higher vorticity extends from $r* = 2$ at 1 km outward and upward to $r* = 3$ at 7 km, in the same radial band as the low-level reflectivity peak described above.

The radius–height profile of divergence (Fig. 8d) shows divergence maximized in two locations: in the eyewall boundary layer and in the upper regions of the eyewall at 10–12-km altitude, with high values of convergence extending upward along the RMW. Inside the RMW is an axis of divergence, with a local maximum centered at 1-km altitude and another at 12–14-km altitude. The lower divergence maximum is associated with the outflow shown in the radial wind composite (cf. Figs. 7c,d), while the upper-level divergence maximum is associated with air accelerating outward into the eyewall. The presence of divergence along the inner edge of the eyewall suggests that air is constantly being lost to the eyewall. This seems to support the work of Malkus (1958), who postulated that air in the eye had a short residence time, in contrast

to Willoughby (1998), who thought that the air above the inversion in the eye may have been trapped there since the formation of the eyewall. Radially outward from the eyewall the divergence decreases, but within $r* = 2$–3 there is an indication of lower-tropospheric convergence situated underneath upper-level divergence, with the zero line located at about the melting level.

The presence of increased axisymmetric reflectivity and vertical velocity in the $r* = 2$–3 band, along with the axis of elevated vorticity extending radially outward with height and the updraft/downdraft couplet in this same radial band, is broadly consistent with the structures shown in the National Center for Atmospheric Research (NCAR) Electra Doppler Radar (ELDORA) observations of Hurricanes Katrina and Rita (Hence and Houze 2008). The results shown here suggest that the $r* = 2$–3 radial band is a preferred region for either rainbands or secondary eyewalls (or a combination of the two). These features can also be seen in many of the lower-fuselage

radar composites shown in Fig. 1. While no definitive explanation for the formation of rainbands and secondary eyewalls, and why they would be preferred in the $r^* = 2$–3 band, has been provided in the literature, several hypotheses have been advanced. These include the suggestion that 1) the development of these features is related to downdraft-induced convergence from the primary eyewall and upper-level subsidence in the outward branch of the secondary circulation (e.g., Willoughby et al. 1982); 2) it is driven by the axisymmetrization of outward-propagating vortex Rossby waves that reach their stagnation radius (Montgomery and Kallenbach 1997); 3) it develops where there is an overlap of sufficiently high vorticity in a "beta skirt," sufficiently high ambient convective available potential energy, and long filamentation time scales to support the development of a secondary eyewall (Terwey and Montgomery 2008); and 4) it occurs where there is Ekman pumping caused by a tilt of the outer vortex in the presence of vertical shear that leads to the development of a stationary band (Reimer et al. 2010).

c. Variability of vortex-scale fields

The variability about the symmetric structure for storms in the sample is provided in Fig. 9, which shows the standard deviations for the tangential wind, radial wind, vertical wind, and relative vorticity. The standard deviation of tangential wind (Fig. 9a) shows maxima inside the eyewall ($r^* = 0.3$–0.5), along the inner edge of the eyewall at altitudes above 5 km, and in the $r^* = 2$–3.5 radial band. It also shows a minimum between $r^* = 1$ and 2. The maximum inside the eyewall is likely tied to differences in the shape of the radial profile of tangential wind for these storms (e.g., U-shaped vs V-shaped profiles; Kossin and Eastin 2001), while the maximum in the higher altitudes along the inner eyewall indicate differences in the decay of tangential winds with height along the RMW. The outer peak in tangential wind variability is likely related to the presence of rainbands and secondary eyewalls, which is consistent with the peaks in reflectivity, radial wind, vorticity, and divergence seen in the mean fields (cf. Figs. 7–8).

Radial wind variability from the profile analyses is shown in Fig. 9b. There is maximum variability in the inflow layer, along and just outside the eyewall, and in the $r^* = 2.5$–3.5 radial band above 2-km altitude, coincident with the secondary peak in outflow seen in the axisymmetric mean (cf. Fig. 7d). Differences in the inflow-layer depth and strength across storms are likely responsible for the peak in variability in the inflow layer. While the magnitude of the standard deviation is largest in the low-level inflow layer, it is ~50% or less of the magnitude of the mean radial flow there and also in the area of enhanced outflow at ~2 km inside the RMW (Fig. 9b), indicating

that these are persistent and robust features. In terms of the percentage of the mean, the variability is maximized along the eyewall and in the $r^* = 2.5$–3.5 band. Differences in eyewall width and slope are likely responsible for the eyewall peak, while differences in the presence/absence, radial location, and convective activity of rainbands and secondary eyewalls are likely responsible for the peak at $r^* = 2.5$–3.5.

The standard deviation of the vertical velocity field from the profiles (Fig. 9c) shows three local maxima: inside the RMW through the depth of the troposphere, between 2- and 6-km altitude just outside the RMW, and between 2 and 6 km in the $r^* = 2.5$–3.5 radial band. The maxima inside and at the RMW are associated with differences in the magnitude and width of the symmetric eyewall updraft. The maximum just outside the eyewall is coincident with the symmetric downdraft in the midtroposphere outside the eyewall seen in the profile composite mean (cf. Fig. 7f). Standard deviation values are generally much larger than the composite mean value, but that largely reflects the fact that the vertical velocity is fairly symmetrically distributed around 0, especially outside the eyewall (shown later in section 3d). The peak outside $r^* = 2.5$ is again likely tied to rainbands and secondary eyewalls.

The variation in relative vorticity calculated from the swath analyses (Fig. 9d) shows a maximum at the peak vorticity along the inner edge of the eyewall and a secondary, weaker maximum at $r^* = 2$–2.5. Between these two maxima is a relative minimum in variability. The eyewall peak is likely associated with variations in eyewall structure across storms (e.g., the radial gradient of tangential velocity along the inner eyewall edge; e.g., Kossin and Eastin 2001). While the magnitude of the variability is maximized inside the eyewall, as a percentage of the mean the variability is a minimum. This reflects the large value of vorticity in the composite mean (cf. Fig. 8c) and the persistence and robustness of this feature. As a percentage of the mean, the secondary peak at $r^* = 2$–2.5 is maximized. This increase in variability is likely tied to the low background value of vorticity at these radii and to the presence or absence of rainbands and secondary eyewalls, which have been shown to contain positive vorticity in the low- to midtroposphere (e.g., Hence and Houze 2008).

In addition to the inherent storm-to-storm structural variability mentioned above, there are two possible sources of variability in these composites, particularly at and near the eyewall: variability in the eyewall slopes, and data coverage problems leading to significant variations in sample size in r^*–z space. To address the first possible source, the compositing analysis was recalculated for the swaths, only with the fields normalized based on
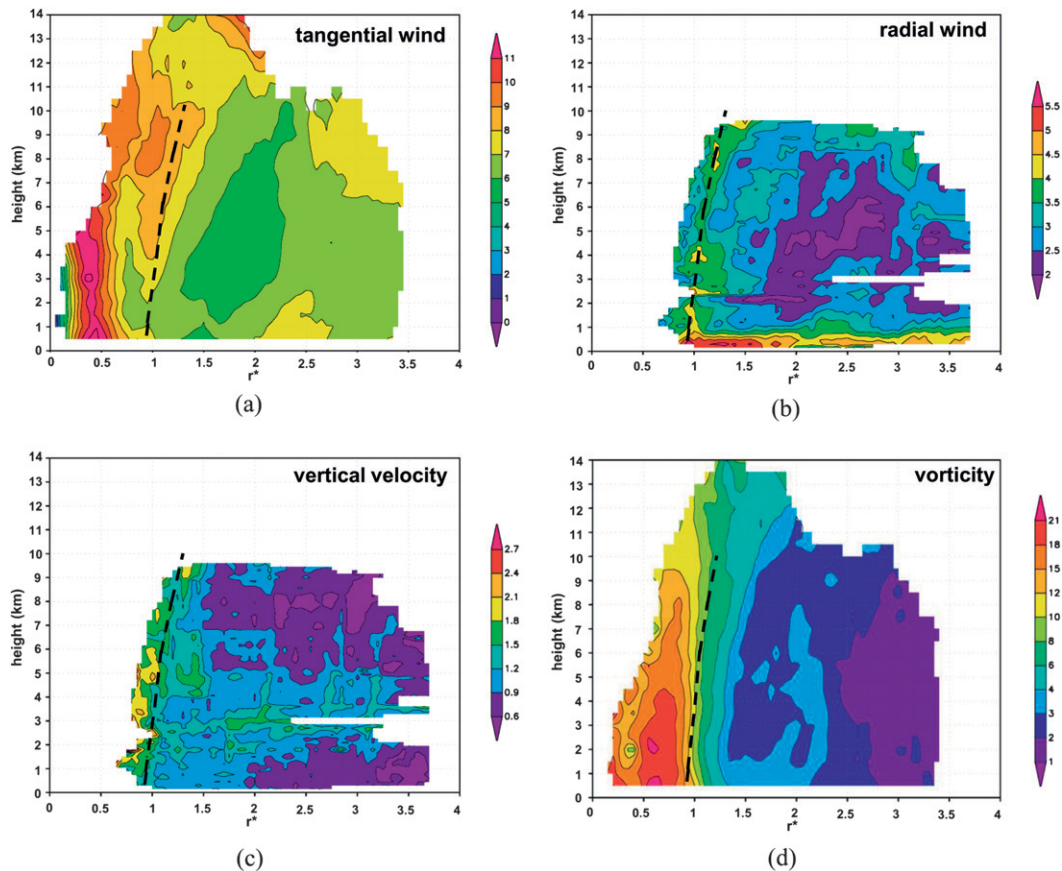
FIG. 9. (a) Standard deviation of tangential wind (m s^{-1}) using swath composite. (b) As in (a), but for radial wind (m s^{-1}) using profile composite. (c) As in (a), but for vertical wind (m s^{-1}) using profile composite. (d) As in (a), but for relative vorticity ($\times 10^{-4}$ s^{-1}) using swath composite. The dashed lines denote the axis of peak axisymmetric tangential wind from 0.5- to 10-km altitude calculated from the swath composite in Fig. 7a.

the radius of maximum axisymmetric wind at each level, instead of a single level. This calculation accounted for the variability in eyewall slope from analysis to analysis. A comparison of the standard deviation in this plot and one normalized to RMW_2km (not shown) indicates little difference between the variability at and within the eyewall, suggesting that variations in eyewall slope from swath to swath were not a major contributor to the variability shown here. To address the second possible source of increased variability, a plot of sample size was made for the vertical velocity and vorticity profiles (not shown). In several locations in r^*–z space, the location of peak variance is along the boundary of the plotted field, indicating that this is where the sample size is near 20 (since 20 was the minimum threshold for plotting the means and variances). In other locations, however, the variance and standard deviation are maximized away from the periphery of the plot, where the sample sizes are up to 50%–75% larger. Thus, data coverage limitations may explain some of the variance, particularly along the edge of the

plots, but there are several locations of high variance that are also within areas of comparatively large data coverage. For these reasons, it is felt that the variances of radial wind, vertical velocity, and relative vorticity are largely reflecting the third possible source of variance (i.e., actual variability in the structure of these parameters from analysis to analysis) and are not simply reflections of eyewall slope variability or data coverage limitations.

d. Convective-scale properties

Statistics of reflectivity, vertical velocity, and relative vorticity are calculated from the composites to show the structure of convective-scale features within the composite storm. To examine how these statistics vary as a function of proximity to the RMW, the radial dimension is divided into six regions, shown in Table 4. These regions are roughly meant to depict the eye (region 1), inner eyewall edge (region 3), outer eyewall edge (region 4), and outer radii (region 6), and the transition zones among them (regions 2 and 5). Two regions are highlighted here

for the differences in their convective-scale structures: the inner eyewall edge (region 3) and the outer radii (region 6).

Vertical profiles calculated from the swaths of mean vertical velocity, reflectivity, and vorticity for these two regions are shown in Figs. 10–12. Not surprisingly, the mean vertical velocity along the inner eyewall is higher than in the outer radii (Fig. 10a). Mean vertical velocity steadily increases from 1 m s^{-1} at 1-km altitude to a peak values ~ 1.5 m s^{-1} at 6 km. It decreases slightly above that before returning to its peak value by 10-km altitude. The double peak of this inner eyewall profile is generally consistent with that of Black et al. (1996),[3] who show a peak in vertical velocity at a low altitude, with values decreasing significantly above the melting level before increasing slightly (though weaker than in the composites shown here) in the upper troposphere in their ''eyewall'' region (their Fig. 9b).

There are several possible explanations for the weaker upper-level vertical velocity seen in Black et al. (1996) compared with the composites shown here. First, Black et al. (1996) subjectively determined the eyewall based on reflectivity features. As a result, the radial region encompassing the eyewall extends farther outward than what is done here. By extending their eyewall definition farther outward, their eyewall vertical velocity profiles include regions of weaker updrafts just outside the eyewall. By contrast, the vertical profiles shown here extend from $r* = 0.75$–1, which only includes the strongest updrafts as shown in Figs. 7e,f. Indeed, the peak updrafts in the vertical profile shown here, at 6–12-km altitude, are consistent with the peak updrafts shown in Fig. 7e. Another possible source of difference between the vertical velocity profiles shown here and in Black et al. (1996) is the method in which vertical velocity is calculated. Black et al. (1996) estimated vertical velocity from examining the radar beam when it was at vertical incidence, so most of the uncertainty in the vertical velocity retrieval is in the estimate of fall speed. Vertical velocities from the swath data, by contrast, use a continuity constraint in conjunction with fall speed estimates to derive vertical velocity (see discussion in section 2c). A third possible reason why the updrafts in this dataset are stronger than that in Black et al. (1996) is that the

aircraft often maneuvers to avoid convective cores, so the vertically incident data used in Black et al. (1996) would have missed the maximum updrafts. The vertical velocity profile for the outer radii shows much weaker velocities than the inner eyewall, with maximum values reaching 0.3 m s^{-1} at 6-km altitude. This contrasts with the profile in the ''stratiform'' region of Black et al. (1996) in that there is no lower-tropospheric downdraft in the mean. This may be due to the difference in vertical velocity calculations, but also to the fact that the profiles in the outer radii shown here include all radial regions where $r* > 1.5$. This would include any outer eyewalls and rainbands that may exist at these radii, which would alter the mean profiles.

The vertical variation of the distribution of vertical velocity from these two regions is shown using CFADs (Figs. 10b,c). The CFAD for the inner eyewall shows a broad spectrum of updrafts and downdrafts, with peak updraft values reaching 10 m s^{-1} at 6-km altitude and peak downdrafts of -7 m s^{-1} at 3 km. The bulk of the distribution (15%–30%), though, is found between -1 and 3 m s^{-1}. Modal values are between 1 and 2 m s^{-1} and reach a peak around 6 km, similar to the mean profile shown in Fig. 10a. This distribution is generally consistent with eyewall vertical velocities found in vertical incidence radar data (Black et al. 1996) and flight-level data (Jorgensen 1984; Jorgensen et al. 1985). The strongest up- and downdrafts seen in the distributions shown here and the previous work are indicative of what Malkus and Riehl (1960) and Simpson et al. (1998) identified as hot towers, which are deep, undilute convective cores in the eyewall. These hot towers, driven by local buoyancy (Smith et al. 2005), accomplish a significant portion of the vertical mass flux in the eyewall (Braun 2002; Fierro et al. 2009; Rogers 2010). As mentioned above, though, the bulk of the distribution consists of weak drafts. This is consistent with what Emanuel (1986) and Rotunno and Emanuel (1987) theorized (i.e., that TC maintenance and intensification occur in a state of near-symmetric neutrality, with the minimum central pressure determined by sea surface temperature and the temperature of the outflow layer). In a study of flight-level observations from multiple storms, Eastin et al.

TABLE 4. List of radial bands and regions used in calculation of convective-scale statistics.

Radial band	Region
1: $r* < 0.5$	Eye
2: $0.5 \le r* < 0.75$	(Transition zone)
3: $0.75 \le r* < 1$	Inner eyewall edge
4: $1 \le r* < 1.25$	Outer eyewall edge
5: $1.25 \le r* < 1.5$	(Transition zone)
6: $1.5 \le r*$	Outer radii

---

[3] The vertical profiles shown here are calculated by assuming a vertically oriented boundary between regions (i.e., they do not account for eyewall slope). In high-gradient regions such as along the eyewall inner edge, they likely include some mixture of air radially inside the eyewall and within the eyewall itself, which may obscure some of the signal. However, this is consistent with the calculation methodology of Black et al. (1996) and was maintained here.
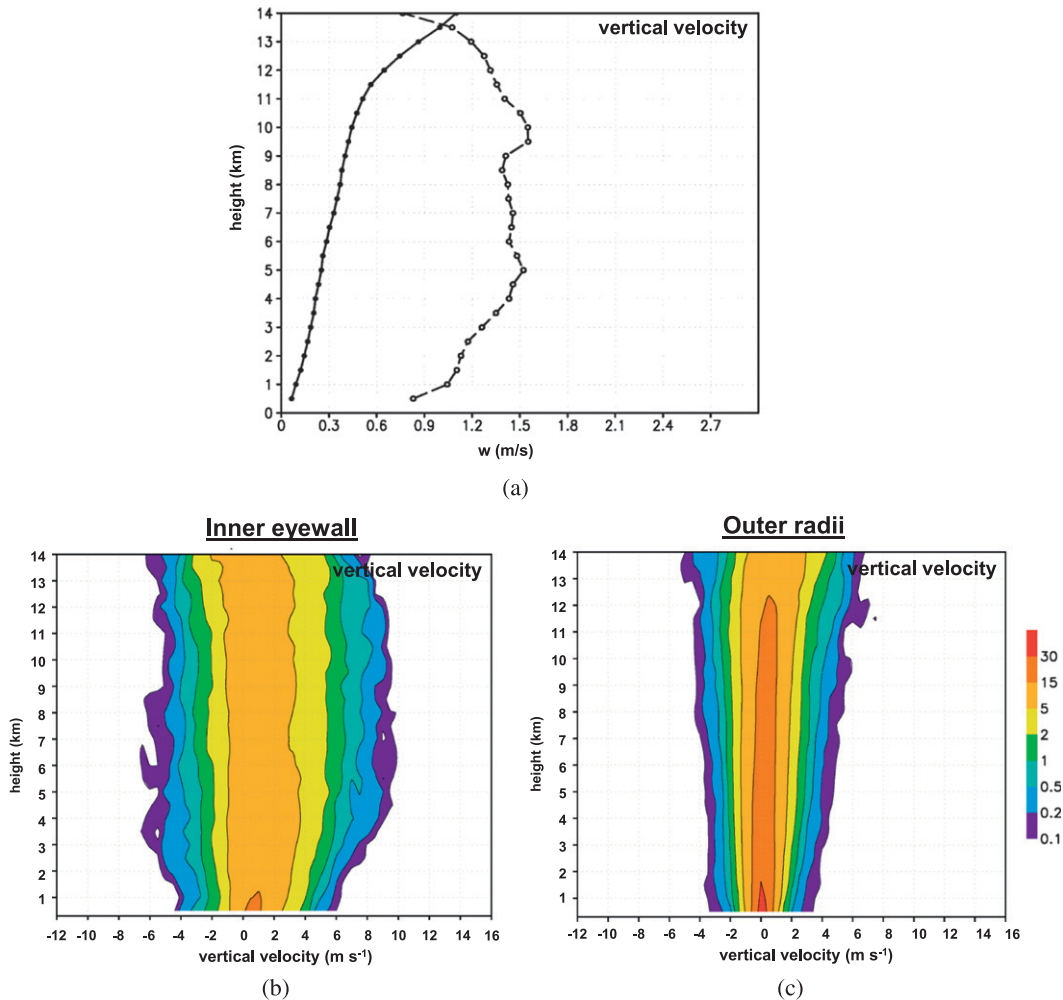
FIG. 10. (a) Vertical profiles of swath-based composite mean of vertical velocity (m s^{-1}) for inner eyewall edge (dotted) and outer radii (solid). (b) CFAD of vertical velocity (shaded, %) for inner eyewall region. (c) As in (b), but for outer radii.

(2005a) found that eyewall vertical motion was a combination of both buoyantly driven (strong) updrafts and (weak) slantwise-neutral ascent. This interpretation is consistent with what is shown in these distributions. The CFAD of vertical velocity for the outer radii (Fig. 10c) shows a narrower distribution of vertical velocities than in the eyewall, with peak up- and downdrafts of 5 and -4 m s^{-1}, respectively, and the bulk of the distribution between -1 and 1 m s^{-1}. This distribution is again consistent with the Black et al. (1996) vertical incidence measurements for stratiform regions, indicating that this radial region is primarily associated with stratiform processes. The small percentage of updrafts >4–5 m s^{-1} in this radial band may indicate the presence of outer eyewalls or rainband activity, as suggested in Figs. 7–9.

The reflectivity vertical profile shown in Fig. 11a indicates that the reflectivity in the inner eyewall is higher than the outer radii over much of the troposphere, by a value ranging between 2 and 6 dBZ. The inner eyewall profile is similar to that shown by Black et al. (1996), except that the reflectivity at the 2–4-km altitude is higher in the profiles shown here than in that shown in Black et al. (1996). The reflectivity in the outer radii also shows a clearer indication of a bright band at the 4.5–5-km altitude than that shown in the inner eyewall. This is indicative of more stratiform processes occurring in this radial range (e.g., Black et al. 1996; Marks and Houze 1987).

Peak eyewall reflectivity from the CFAD shown in Fig. 11b reaches 55 dBZ in the lower troposphere, compared with peak values of 50 dBZ for the outer radii (Fig. 11c). The mode of the distributions shows a comparable difference, with the mode for the eyewall around 35 dBZ and linearly decreasing across the melting level above
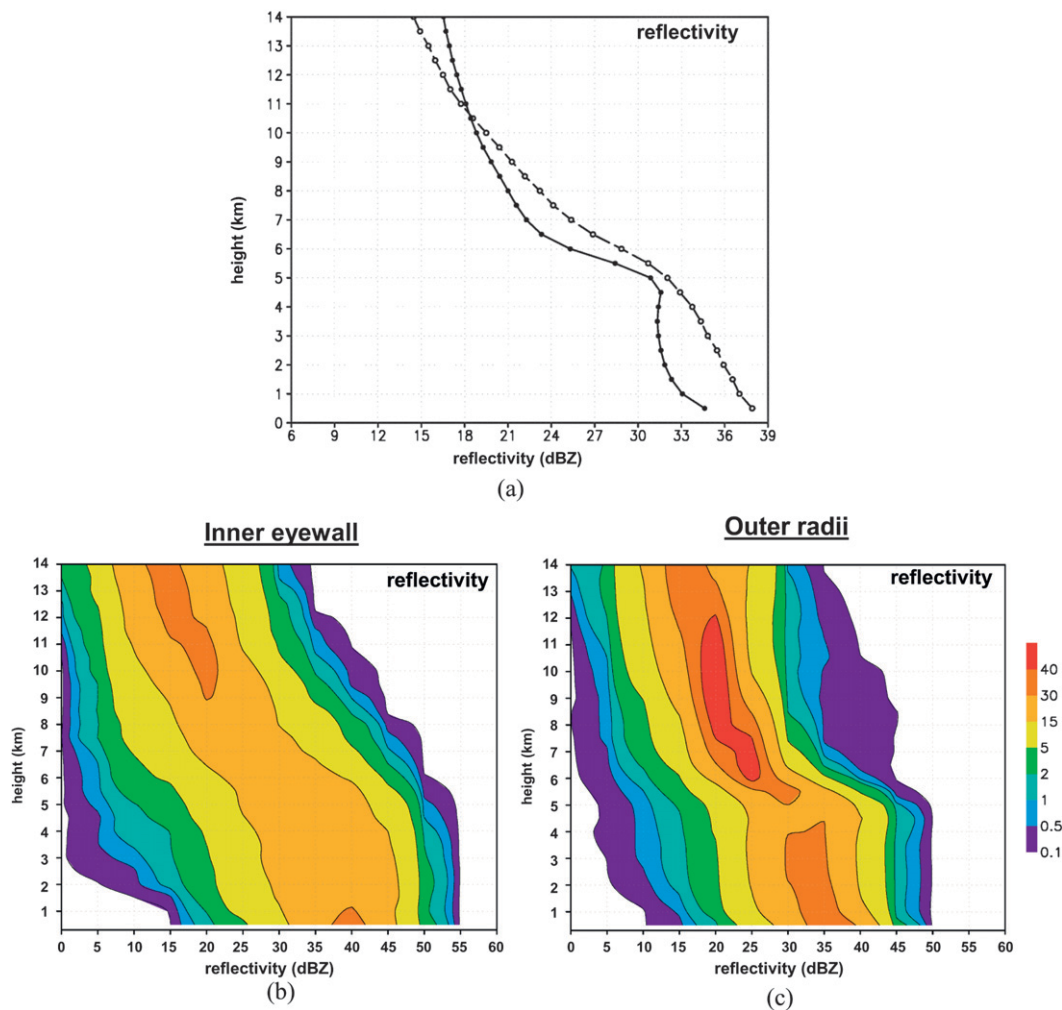
FIG. 11. (a) Vertical profiles of swath-based composite mean of reflectivity (dBZ) for inner eyewall edge (dotted) and outer radii (solid). (b) CFAD of reflectivity (shaded, %) for inner eyewall region. (c) As in (b), but for outer radii.

5-km altitude. By contrast, the reflectivity for the outer radii shows a sharper drop above the bright band at the melting level, similar to the mean profile from Fig. 11a and again indicative of the dominance of stratiform rain processes in this radial range. The ~5-dBZ difference between the eyewall and outer radii reflectivity distribution continues above the melting level up to 12–14-km altitude, for nearly all portions of the distribution. The general differences in the reflectivity distributions between the inner eyewall and outer radii identified here (i.e., ~5-dBZ difference, sharper drop above melting level for outer radii) are broadly consistent with differences in reflectivity distributions for the eyewall and inner rainband regions seen in a composite of the Tropical Rainfall Measuring Mission (TRMM) overpasses (Cecil et al. 2002). Modal values from the Doppler composite are about 5–7 dBZ higher than the median values from the TRMM dataset for both regions when all points are considered from the TRMM dataset.

When only ''convective certain'' points are considered from TRMM, the Doppler composite values are about 2 dBZ less for the inner eyewall and about 5 dBZ less for the outer radii. This suggests that both a mix of convective and stratiform precipitation occurs, but a higher proportion of the precipitation is stratiform in the outer radii compared with the inner eyewall.

The vertical profile of vorticity in Fig. 12a shows marked differences between the inner eyewall and outer radii. Peak vorticity reaches 35×10^{-4} s^{-1} at 1-km altitude and decreases steadily to near 20×10^{-4} s^{-1} by 10-km altitude. The outer radii has much lower vorticity that does not exceed 5×10^{-4} s^{-1} from 500-m up to 12-km altitude. The difference between these two radial regions is consistent with the significant radial gradient in vorticity between the eyewall and outer radii seen in Fig. 8c and that shown in Kossin and Eastin (2001) and Mallen et al. (2005). The vorticity CFADs (Figs. 12b,c) show that
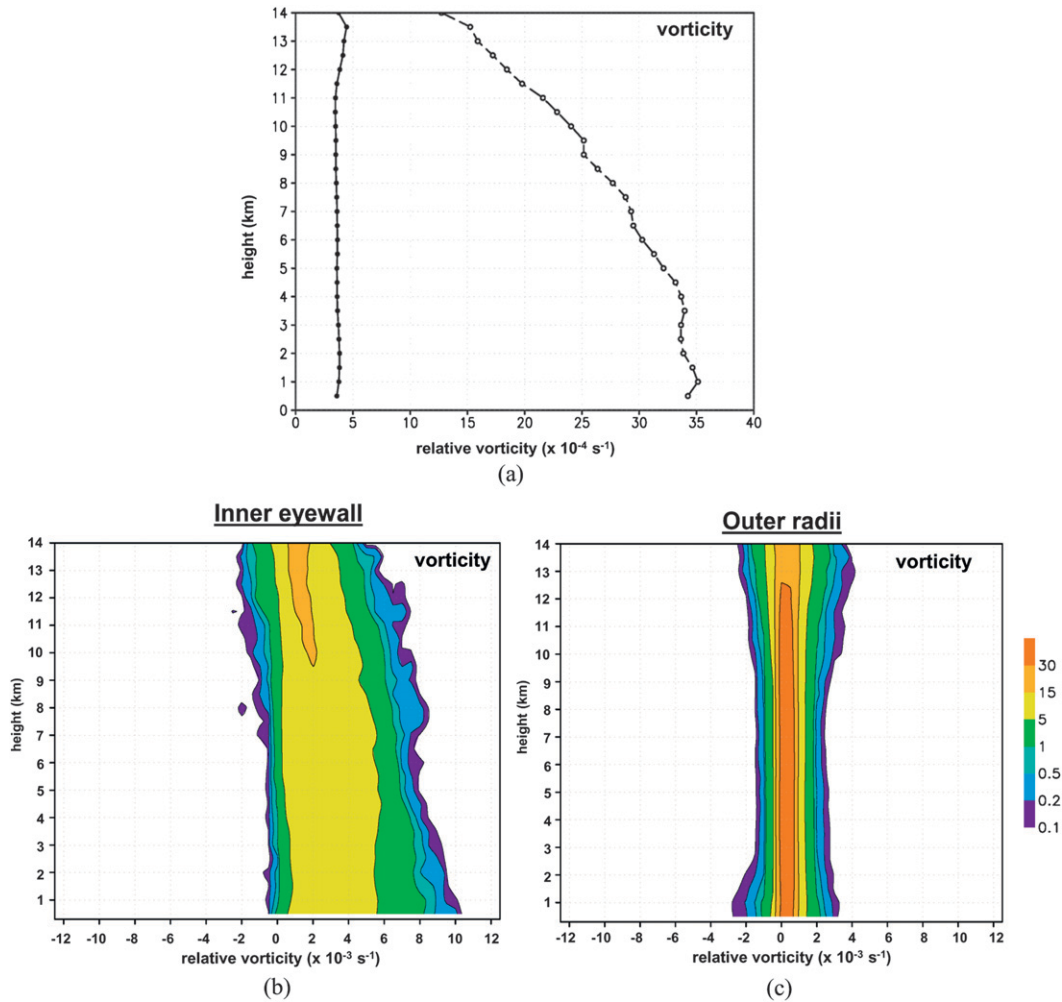
FIG. 12. (a) Vertical profiles of swath-based composite mean of vertical vorticity ($\times10^{-4}$ s^{-1}) for inner eyewall edge (dotted) and outer radii (solid). (b) CFAD of vertical vorticity (shaded, %) for inner eyewall region. (c) As in (b), but for outer radii. Note difference in exponent in magnitude of vorticity for CFADs compared to mean profile.

the distribution of vorticity along the eyewall inner edge is positively skewed, particularly in the lower troposphere below 4 km. Peak values of lower-tropospheric vorticity can reach 1×10^{-2} s^{-1} in the eyewall, while there are generally very few (<0.5%) areas with negative vorticity below 10 km. This vorticity distribution indicates the dominance of cyclonic vorticity within the eyewall and the presence of cores of extremely high vorticity possibly associated with vortical hot towers (VHTs; Montgomery et al. 2006b). Modal values of eyewall vorticity steadily decrease with height, from 3×10^{-3} s^{-1} near the surface to 2×10^{-3} s^{-1} at 12-km altitude, indicating the weakening of the vortex with height. In the outer radii, by contrast, the distribution is narrower and less skewed. Peak values reach 4×10^{-3} s^{-1}, and there is a sizable portion of the vorticity distribution (~30%) that is negative below 10 km. The distribution also varies little with height.

e. Turbulent-scale properties

The compositing of radar data can also help better understand the turbulent structure and processes of TCs. TC's turbulent properties, especially in the hurricane boundary layer, can provide information on intensity and intensity change (Malkus and Riehl 1960; Emanuel 1986, 1995). However, collecting turbulence data can be challenging because of instruments' lack of high temporal or spatial resolution and because some areas, such as the hurricane boundary layer (HBL), are often not accessible because of safety concerns. Lorsolo et al. (2010) designed a method to retrieve TC TKE by taking advantage of the high resolution of the WP-3D tail Doppler radar. The TKE retrieval using Doppler radar measurements provides a unique opportunity to assess turbulent energy throughout the storm. In Lorsolo et al. the analysis is

based on the fact that the Doppler measurement can be expressed as the sum of the mean radial velocity over a grid cell and a turbulent part. The turbulent part is represented by the variance of measurements of ~150-m spatial resolution about the mean Doppler radial velocity of a 10 km (across flight track) × 1.5 km (along flight track) × 0.15 km (vertical) grid cell centered on the flight track. To compute TKE the profile values of all three wind components are determined from all the 150-m range gates within a profile volume. The projection of this velocity is then subtracted from all the individual range-gate observations to determine a residual radar-radial velocity variance that represents the TKE. Although the method cannot capture the far (blue) end of the spectrum, the fine bin spacing allows the resolution of the energy associated with small scales of motion.

Lorsolo et al. (2010) used the compositing method with a similar dataset as in the present study (their Fig. 7) and showed two primary regions with relatively high TKE (Fig. 13)—in the boundary layer outside of the RMW and within and just along the inner edge of the eyewall. The highest values are located at $r^* = 0.75$ below 2 km and could be related to the high gradient in radial wind occurring here (cf. Fig. 7d). A secondary maximum in TKE is evident at $r^* = 2$–2.5 between the surface and 6-km altitude, reflecting other areas of stronger turbulence (e.g., rainbands and secondary eyewalls). This is generally consistent with the secondary peak in vorticity variability shown in Fig. 9d. The analysis suggests that TKE can be an effective diagnostic tool to assess the dynamical boundary depth as it can be challenging to estimate (e.g., Zhang et al. 2011a). The high values of TKE in the HBL and in the eyewall imply that turbulent energy is being injected into the eyewall region to supplement the already existing turbulent energy as mentioned by Smith and Montgomery (2010).

The difference in structure between the inner eyewall and outer radii is also apparent in the TKE field. Figure 14 presents mean vertical profiles of TKE for the inner eyewall and outer radii (i.e., regions 3 and 6). In the outer radii there is a rapid decrease from 0.15-km altitude to 2 km followed by a steadier decrease to 1 m^2 s^{-2} above that. In the inner eyewall, above 2 km there is also a steady decrease, with as expected higher values of turbulence. However, below 2 km there is a sharp increase in TKE, indicative of strong turbulence in this area. This behavior of the TKE toward and at the RMW suggests that it is related to both horizontal shear and convective processes. In the outer radii, TKE values are smaller, even in the presence of rainbands and secondary eyewalls, which could be due to weaker shear even with a greater buoyancy in these areas. CFADs of TKE for regions 3 and 6 (Fig. 15) show a broad distribution in
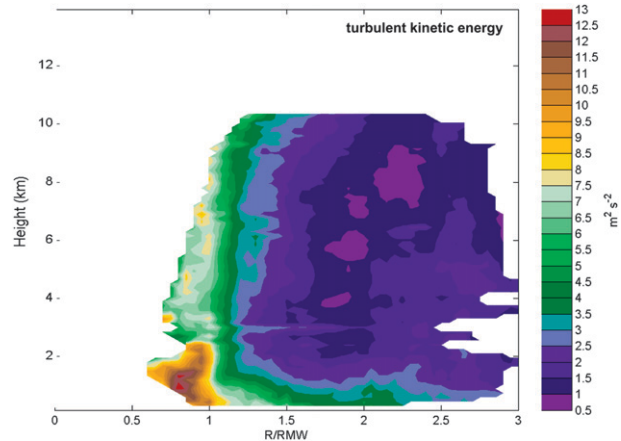

FIG. 13. Composite of turbulent kinetic energy (shaded, m^2 s^{-2}) calculated from profile data.

the inner eyewall (region 3), with values reaching as high as 20 m^2 s^{-2} and modal values generally around 8 m^2 s^{-2} and decreasing with height. In the outer radii (Fig. 15b), the distribution is much more compact. Modal values are around 3 m^2 s^{-2} in the lower troposphere and decrease to 1 m^2 s^{-2} in the upper levels. These results are consistent with those presented by Zhang et al. (2011b), who found similar TKE values in the eyewall and noticed a similar drop of the turbulence energy outside the eyewall region.

4. Summary and conclusions

For the first time, composites of TC inner-core structure deduced from airborne Doppler radar data collected in multiple TCs have been created. These composites depict structures across multiple scales, including the vortex, convective, and turbulent scales. The composites produce many of the structures seen in past case studies, including details of the vortex-scale primary and secondary circulation and distributions of convective- and turbulent-scale properties as a function of proximity to the radius of maximum wind. The ability of these composites to depict many of the structures seen in case studies provides confidence in their accuracy. They provide a spectrum of possible TC structures that complements well the case-study approach. They can also provide context by indicating the representativeness of individual case studies.

The advantages and disadvantages of the swath versus the profile method for estimating winds was discussed. The profile method has a higher vertical resolution and captures the inflow boundary layer far better than the swath method. This is an important result since most prior work has used the swath method from an altitude
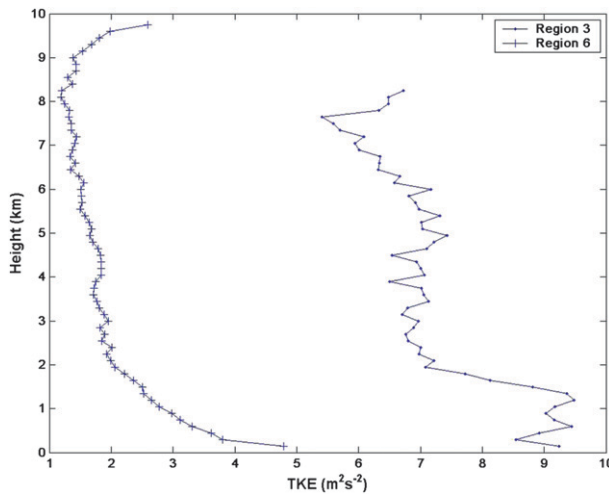
FIG. 14. Vertical profiles of composite mean turbulent kinetic energy for inner eyewall edge (dotted) and outer radii (crosses).

where the lowest 0.5 km is not adequately sampled. The swath method performs best for the upper troposphere and in the eye, as well as providing better coverage azimuthally. However, its reliance on the continuity constraint introduces another source of uncertainty in the calculation of vertical velocity.

The composites capture the axisymmetric tangential wind peak, including its outward slope and decay with increasing altitude, as seen in several past studies. Key characteristics of the radial circulation, such as inflow concentrated in the lowest 1 km, a deeper layer of weaker inflow outside the RMW, the outflow located at the top of the inflow layer just inside the RMW and extending radially outward, and the upper-level outflow are also produced by these composites. The axisymmetric vertical velocity is peaked just inside the peak tangential wind and reflectivity, dropping to near 0 m s^{-1} just outside this region before increasing again where the stratiform rain is concentrated. The secondary circulation vectors show that the eyewall updraft generally follows angular momentum surfaces, but crosses angular momentum surfaces in the inflow layer, as expected. This pattern is particularly evident in the profile composite, which better depicts the inflow layer due to its higher vertical resolution.

Reflectivity composites show the deep column of high reflectivity associated with the eyewall and a broader horizontal distribution radially outward associated with stratiform precipitation. Axisymmetric vorticity is maximized along the inner edge of the eyewall, also sloping outward with increasing altitude similar to the tangential wind peak. Inside the RMW the vorticity decreases significantly, indicating that a ring of vorticity is present, at least in the mean. Outside the RMW the
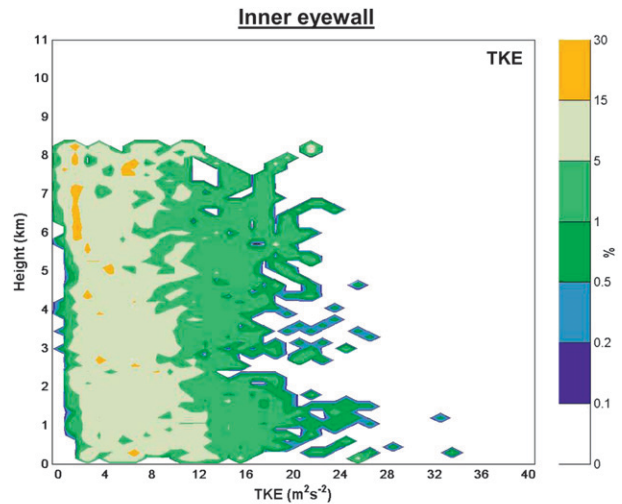
(a)
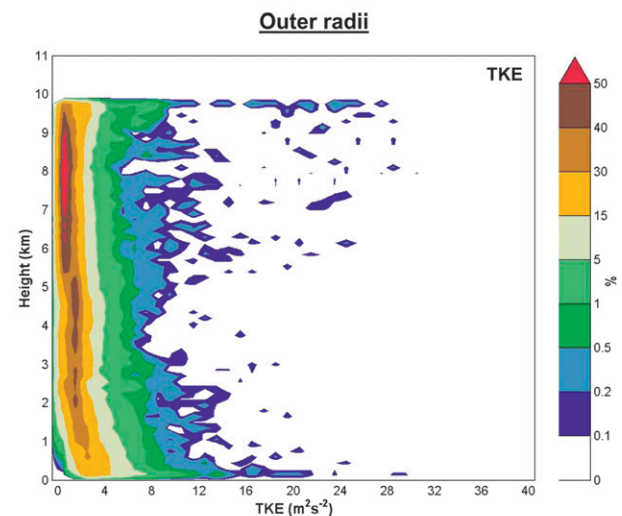
(b)

FIG. 15. CFAD of TKE (shaded, %) for (a) inner eyewall region and (b) outer radii.

vorticity decreases at a rate generally consistent with past studies using individual flight legs, and there is an outer maximum in vorticity at $r* = 2$–3 that is consistent with past case studies of rainbands. Divergence is maximized in two locations: in the eyewall boundary layer and in the upper regions of the eyewall at 10-km altitude. High values of convergence extend upward along the RMW. The lower divergence maximum is associated with an area of enhanced low-level outflow, while the upper-level divergence maximum is associated with air accelerating outward into the eyewall. An outer peak in upper-level divergence and lower-level convergence is located near $r* = 2$–3, near where rainbands and secondary eyewalls are normally located.

Plots of the standard deviation of radial velocity show that the variability is maximized in the low-level inflow, along the eyewall, and in the outer radii near the rainband region. The peak variability in vertical velocity is maximized along the eyewall, just outside the eyewall coincident with weak subsidence in the composite mean, and in the outer radii near where rainbands are likely to exist. The peak variability in relative vorticity is generally maximized near the RMW. This is mostly tied to variations in the magnitude and width of the symmetric eyewall updraft. Another peak in the variability of vorticity is found in the outer radii (i.e., around $r^* = 2$–2.5), which is likely tied to the presence of rainbands in this radial range.

The mean and distribution of vertical velocity, reflectivity, and relative vorticity as a function of proximity to the RMW was also examined. Two regions were selected for closer inspection: the inner eyewall edge and the outer radii. As expected, mean profiles show that vertical velocity, reflectivity, and relative vorticity are all higher in the inner eyewall compared with the outer radii. The distribution of these variables for the inner eyewall and outer radii shows a much broader spectrum of updrafts and downdrafts in the inner eyewall edge compared with the outer radii. Peak up- and downdrafts are stronger along the inner eyewall compared with the outer radii. For reflectivity, the peak values in the lower troposphere are about 5 dBZ higher for the inner eyewall compared with the outer radii. In addition, the reflectivity in the outer radii shows a sharp drop above the bright band at the melting level, again indicative of the dominance of stratiform rain processes in this radial range. For vorticity, the distribution is positively skewed along the inner eyewall, particularly in the lower troposphere, and peak values of low-level vorticity reach 1×10^{-2} s^{-1} with very few areas of negative vorticity. By contrast, the distribution of vorticity in the outer radii is narrower, and a much larger portion of the distribution is negative.

Composites from the radar profiles show the radial distribution of turbulent kinetic energy (TKE). The main regions of high TKE were in the boundary layer outside the RMW and within and just along the inner edge of the eyewall. A clear minimum in TKE is evident just outside the RMW, and a secondary maximum in TKE is seen at about $r^* = 2$–2.5, coincident with enhanced vertical velocity, relative vorticity, and the variance of these two quantities.

There are many possible applications for this compositing methodology. For example, composites of systems exhibiting similar characteristics, such as subsequent rapid intensification (RI) or nonintensification or encounters with vertical shear of different magnitudes and directions, can be compared to determine if there are statistically significant structural differences between the datasets. Preliminary comparisons of composites of TCs that underwent RI with those that remained steady state show some key differences in the vortex- and convective-scale structures. This work will continue. Doppler radar composites can also be used to evaluate model composites from simulations using variable horizontal and vertical resolution or physical parameterizations. Correlations and covariances can also be calculated from the composites that can be used in ensemble-based data assimilation schemes such as the ensemble Kalman filter.

The work shown here has primarily focused on the axisymmetric structure of the vortex and the distribution of convective- and turbulent-scale properties within this axisymmetric framework. Future work will examine the asymmetric structure of the storms as revealed by composites. The asymmetry amplitude can be composited easily, but the asymmetry phase will be more challenging. A method for normalizing the radar analyses is required for such a calculation. One possibility is to normalize by asymmetry phase, or to normalize by processes known to drive low-wavenumber asymmetries, such as storm translation or vertical shear. Finally, additional observational datasets will be added to these composites. In particular, the addition of GPS dropsonde data to the composites will allow a determination of the composite thermodynamic structures in these TCs, especially in the boundary layer.

REFERENCES

Aberson, S. D., M. L. Black, R. A. Black, J. J. Cione, C. W. Landsea, F. D. Marks, and R. W. Burpee, 2006a: Thirty years of tropical cyclone research with the NOAA P-3 aircraft. *Bull. Amer. Meteor. Soc.,* **87,** 1039–1055.

——, ——, M. T. Montgomery, and M. Bell, 2006b: Hurricane Isabel (2003): New insights into the physics of intense storms. Part II: Extreme localized wind. *Bull. Amer. Meteor. Soc.,* **87,** 1349–1354.

Baker, A. K., M. D. Parker, and M. D. Eastin, 2009: Environmental ingredients for supercells and tornadoes within Hurricane Ivan. *Wea. Forecasting,* **24,** 223–244.

Barnes, G. M., and M. D. Powell, 1995: Evolution of the inflow boundary layer of Hurricane Gilbert (1988). *Mon. Wea. Rev.,* **123,** 2348–2368.

——, E. J. Zipser, D. Jorgensen, and F. Marks Jr., 1983: Mesoscale and convective structure of a hurricane rainband. *J. Atmos. Sci.,* **40,** 2125–2137.

Bell, M. M., and M. T. Montgomery, 2008: Observed structure, evolution, and potential intensity of category 5 Hurricane Isabel (2003) from 12 to 14 September. *Mon. Wea. Rev.,* **136,** 2023–2046.

Black, M. L., R. W. Burpee, and F. D. Marks Jr., 1996: Vertical motion characteristics of tropical cyclones determined with airborne Doppler radial velocities. *J. Atmos. Sci.,* **53,** 1887–1909.

——, J. F. Gamache, F. D. Marks, C. E. Samsury, and H. E. Willoughby, 2002: Eastern Pacific Hurricanes Jimena of 1991 and Olivia of 1994: The effect of vertical shear on structure and intensity. *Mon. Wea. Rev.,* **130,** 2291–2312.

Black, P. G., and Coauthors, 2007: Air–sea exchange in hurricanes: Synthesis of observations from the Coupled Boundary Layer Air–Sea Transfer Experiment. *Bull. Amer. Meteor. Soc.,* **88,** 357–374.

Braun, S. A., 2002: A cloud-resolving simulation of Hurricane Bob (1991): Storm structure and eyewall buoyancy. *Mon. Wea. Rev.,* **130,** 1573–1592.

——, M. T. Montgomery, K. J. Mallen, and P. D. Reasor, 2010: Simulation and interpretation of the genesis of Tropical Storm Gert (2005) as part of the NASA Tropical Cloud Systems and Processes Experiment. *J. Atmos. Sci.,* **67,** 999–1025.

Cecil, D. J., E. J. Zipser, and S. W. Nesbitt, 2002: Reflectivity, ice scattering, and lightning characteristics of hurricane eyewalls and rainbands. Part I: Quantitative description. *Mon. Wea. Rev.,* **130,** 769–784.

Cione, J. J., P. G. Black, and S. H. Houston, 2000: Surface observations in the hurricane environment. *Mon. Wea. Rev.,* **128,** 1550–1561.

Didlake, A. C., and R. A. Houze, 2009: Convective-scale downdrafts in the principal rainband of Hurricane Katrina (2005). *Mon. Wea. Rev.,* **137,** 3269–3293.

Dodge, P., R. W. Burpee, and F. D. Marks Jr., 1999: The kinematic structure of a hurricane with sea level pressure less than 900 mb. *Mon. Wea. Rev.,* **127,** 987–1004.

Drennan, W. M., J. A. Zhang, J. R. French, C. McCormick, and P. G. Black, 2007: Turbulent fluxes in the hurricane boundary layer. Part II: Latent heat flux. *J. Atmos. Sci.,* **64,** 1103–1115.

Eastin, M. D., and M. C. Link, 2009: Miniature supercells in an offshore outer rainband of Hurricane Ivan (2004). *Mon. Wea. Rev.,* **137,** 2081–2104.

——, W. M. Gray, and P. G. Black, 2005a: Buoyancy of convective vertical motions in the inner core of intense hurricanes. Part I: General statistics. *Mon. Wea. Rev.,* **133,** 188–208.

——, ——, and ——, 2005b: Buoyancy of convective vertical motions in the inner core of intense hurricanes. Part II: Case studies. *Mon. Wea. Rev.,* **133,** 209–227.

Emanuel, K. A., 1986: An air–sea interaction theory for tropical cyclones. Part I: Steady-state maintenance. *J. Atmos. Sci.,* **43,** 585–605.

——, 1995: Sensitivity of tropical cyclones to surface exchange coefficients and a revised steady-state model incorporating eye dynamics. *J. Atmos. Sci.,* **52,** 3969–3976.

Fierro, A. O., R. F. Rogers, F. D. Marks, and D. S. Nolan, 2009: The impact of horizontal grid spacing on the microphysical and kinematic structures of strong tropical cyclones simulated with the WRF-ARW model. *Mon. Wea. Rev.,* **137,** 3717–3743.

Frank, W. M., 1982: Large-scale characteristics of tropical cyclones. *Mon. Wea. Rev.,* **110,** 572–586.

Franklin, J. L., S. J. Lord, S. E. Feuer, and F. D. Marks, 1993: The kinematic structure of Hurricane Gloria (1985) determined from nested analyses of dropwindsonde and Doppler radar data. *Mon. Wea. Rev.,* **121,** 2433–2451.

——, M. L. Black, and K. Valde, 2003: GPS dropwindsonde wind profiles in hurricanes and their operational implications. *Wea. Forecasting,* **18,** 32–44.

Gamache, J. F., 1997: Evaluation of a fully three-dimensional variational Doppler analysis technique. Preprints, *28th Conf. on Radar Meteorology,* Austin, TX, Amer. Meteor. Soc., 422–423.

——, R. A. Houze Jr., and F. D. Marks Jr., 1993: Dual-aircraft investigation of the inner core of Hurricane Norbert. Part III: Water budget. *J. Atmos. Sci.,* **50,** 3221–3243.

Gao, J., M. Xue, A. Shapiro, and K. K. Droegemeier, 1999: A variational method for the analysis of three-dimensional wind fields from two Doppler radars. *Mon. Wea. Rev.,* **127,** 2128–2142.

Gray, W. M., and D. J. Shea, 1973: The hurricane's inner core region. II. Thermal stability and dynamic characteristics. *J. Atmos. Sci.,* **30,** 1565–1576.

Hence, D. A., and R. A. Houze Jr., 2008: Kinematic structure of convective-scale elements in the rainbands of Hurricanes Katrina and Rita (2005). *J. Geophys. Res.,* **113,** D15108, doi:10.1029/2007JD009429.

Houze, R. A., Jr., F. D. Marks Jr., and R. A. Black, 1992: Dual-aircraft investigation of the inner core of Hurricane Norbert. Part II: Mesoscale distribution of ice particles. *J. Atmos. Sci.,* **49,** 943–963.

——, and Coauthors, 2006: The Hurricane Rainband and Intensity Change Experiment: Observations and modeling of Hurricanes Katrina, Ophelia, and Rita. *Bull. Amer. Meteor. Soc.,* **87,** 1503–1521.

——, S. S. Chen, B. F. Smull, W.-C. Lee, and M. M. Bell, 2007: Hurricane intensity and eyewall replacement. *Science,* **315,** 1235–1239.

——, W.-C. Lee, and M. M. Bell, 2009: Convective contribution to the genesis of Hurricane Ophelia (2005). *Mon. Wea. Rev.,* **137,** 2778–2800.

Jorgensen, D. P., 1984: Mesoscale and convective-scale characteristics of mature hurricanes. Part I: General observations by research aircraft. *J. Atmos. Sci.,* **41,** 1268–1286.

——, E. J. Zipser, and M. LeMone, 1985: Vertical motions in intense hurricanes. *J. Atmos. Sci.,* **42,** 839–856.

Kossin, J. P., and M. D. Eastin, 2001: Two distinct regimes in the kinematic and thermodynamic structure of the hurricane eye and eyewall. *J. Atmos. Sci.,* **58,** 1079–1090.

Lee, W.-C., and F. D. Marks Jr., 2000: Tropical cyclone kinematic structure retrieved from single-Doppler radar observations. Part II: The GBVTD-simplex center finding algorithm. *Mon. Wea. Rev.,* **128,** 1925–1936.

Lorsolo, S., J. L. Schroeder, P. Dodge, and F. Marks, 2008: An observational study of hurricane boundary layer small-scale coherent structures. *Mon. Wea. Rev.,* **136,** 2871–2893.

——, J. Zhang, F. D. Marks, and J. Gamache, 2010: Estimation and mapping of hurricane turbulent energy using airborne Doppler measurements. *Mon. Wea. Rev.,* **138,** 3656–3670.

Malkus, J. S., 1958: On the structure and maintenance of the mature hurricane eye. *J. Meteor.,* **15,** 337–349.

——, and H. Riehl, 1960: On the dynamics and energy transformations in steady state hurricanes. *Tellus,* **12,** 1–20.

Mallen, K. J., M. T. Montgomery, and B. Wang, 2005: Reexamining the near-core radial structure of the tropical cyclone primary

circulation: Implications for vortex resiliency. *J. Atmos. Sci.,* **62,** 408–425.

Marks, F. D., Jr., 1985: Evolution of the structure of precipitation in Hurricane Allen (1980). *Mon. Wea. Rev.,* **113,** 909–930.

——, and R. A. Houze Jr., 1987: Inner core structure of Hurricane Alicia from airborne Doppler radar observations. *J. Atmos. Sci.,* **44,** 1296–1317.

——, and L. K. Shay, 1998: Landfalling tropical cyclones: Forecast problems and associated research opportunities. *Bull. Amer. Meteor. Soc.,* **79,** 305–323.

——, R. A. Houze Jr., and J. F. Gamache, 1992: Dual-aircraft investigation of the inner core of Hurricane Norbert. Part I: Kinematic structure. *J. Atmos. Sci.,* **49,** 919–942.

——, P. G. Black, M. T. Montgomery, and R. W. Burpee, 2008: Structure of the eye and eyewall of Hurricane Hugo (1989). *Mon. Wea. Rev.,* **136,** 1237–1259.

McTaggart-Cowan, R., L. F. Bosart, J. R. Gyakum, and E. H. Atallah, 2007: Hurricane Katrina (2005). Part I: Complex life cycle of an intense tropical cyclone. *Mon. Wea. Rev.,* **135,** 3905–3926.

Montgomery, M. T., and R. J. Kallenbach, 1997: A theory for vortex Rossby waves and its application to spiral bands and intensity changes in hurricanes. *Quart. J. Roy. Meteor. Soc.,* **123,** 435–465.

——, M. M. Bell, S. D. Aberson, and M. L. Black, 2006a: Hurricane Isabel (2003): New insights into the physics of intense storms. Part I: Mean vortex structure and maximum intensity estimates. *Bull. Amer. Meteor. Soc.,* **87,** 1335–1347.

——, M. Nicholls, T. Cram, and A. Saunders, 2006b: A ''vortical'' hot tower route to tropical cyclogenesis. *J. Atmos. Sci.,* **63,** 355–386.

Neldar, J. A., and R. Mead, 1965: A simplex method for function minimization. *Comput. J.,* **7,** 308–313.

Ooyama, K., 1982: Conceptual evolution of the theory and modeling of the tropical cyclone. *J. Meteor. Soc. Japan,* **60,** 369–380.

Powell, M. D., 1990: Boundary layer structure and dynamics in outer rainbands. Part II: Downdraft modification and mixed layer recovery. *Mon. Wea. Rev.,* **118,** 919–938.

Reasor, P. D., M. T. Montgomery, F. D. Marks Jr., and J. F. Gamache, 2000: Low-wavenumber structure and evolution of the hurricane inner core observed by airborne dual-Doppler radar. *Mon. Wea. Rev.,* **128,** 1653–1680.

——, ——, and L. F. Bosart, 2005: Mesoscale observations of the genesis of Hurricane Dolly (1996). *J. Atmos. Sci.,* **62,** 3151–3171.

——, M. D. Eastin, and J. F. Gamache, 2009: Rapidly intensifying Hurricane Guillermo (1997). Part I: Low-wavenumber structure and evolution. *Mon. Wea. Rev.,* **137,** 603–631.

Riemer, M., M. T. Montgomery, and M. E. Nicholls, 2010: A new paradigm for intensity modification of tropical cyclones: thermodynamic impact of vertical wind shear on the inflow layer. *Atmos. Chem. Phys.,* **10,** 3163–3188.

Rogers, R. F., 2010: Convective-scale structure and evolution during a high-resolution simulation of tropical cyclone rapid intensification. *J. Atmos. Sci.,* **67,** 44–70.

——, and E. Uhlhorn, 2008: Observations of the structure and evolution of surface and flight-level wind asymmetries in Hurricane Rita (2005). *Geophys. Res. Lett.,* **35,** L22811, doi:10.1029/2008GL034774.

——, S. S. Chen, J. Tenerelli, and H. E. Willoughby, 2003: A numerical study of the impact of vertical shear on the distribution of rainfall in Hurricane Bonnie (1998). *Mon. Wea. Rev.,* **131,** 1577–1599.

——, and Coauthors, 2006: The Intensity Forecasting Experiment (IFEX): A NOAA multi-year field program for improving tropical cyclone intensity forecasts. *Bull. Amer. Meteor. Soc.,* **87,** 1523–1537.

——, M. L. Black, S. S. Chen, and R. A. Black, 2007: An evaluation of microphysics fields from mesoscale model simulations of tropical cyclones. Part I: Comparisons with observations. *J. Atmos. Sci.,* **64,** 1811–1834.

Rotunno, R., and K. A. Emanuel, 1987: An air–sea interaction theory for tropical cyclones. Part II: Evolutionary study using a nonhydrostatic axisymmetric numerical model. *J. Atmos. Sci.,* **44,** 542–561.

Shea, D. J., and W. M. Gray, 1973: The hurricane's inner core region. I. Symmetric and asymmetric structure. *J. Atmos. Sci.,* **30,** 1544–1564.

Simpson, J., J. B. Halverson, B. S. Ferrier, W. A. Petersen, R. H. Simpson, R. Blakeslee, and S. L. Durden, 1998: On the role of ''hot towers'' in tropical cyclone formation. *Meteor. Atmos. Phys.,* **67,** 15–35.

Sitkowski, M., and G. M. Barnes, 2009: Low-level thermodynamic, kinematic, and reflectivity fields of Hurricane Guillermo (1997) during rapid intensification. *Mon. Wea. Rev.,* **137,** 645–663.

Smith, R. K., and M. T. Montgomery, 2010: Hurricane boundary-layer theory. *Quart. J. Roy. Meteor. Soc.,* **136,** 1665–1670.

——, ——, and H. Zhu, 2005: Buoyancy in tropical cyclones and other rapidly rotating atmospheric vortices. *Dyn. Atmos. Oceans,* **40,** 189–208.

Squires, K., and S. Businger, 2008: The morphology of eyewall lightning outbreaks in two category 5 hurricanes. *Mon. Wea. Rev.,* **136,** 1706–1726.

Stern, D. P., and D. S. Nolan, 2009: Reexamining the vertical structure of tangential winds in tropical cyclones: Observations and theory. *J. Atmos. Sci.,* **66,** 3579–3600.

Terwey, W. D., and M. T. Montgomery, 2008: Secondary eyewall formation in two idealized, full-physics modeled hurricanes. *J. Geophys. Res.,* **113,** D12112, doi:10.1029/2007JD008897.

Uhlhorn, E. W., and P. G. Black, 2003: Verification of remotely sensed sea surface winds in hurricanes. *J. Atmos. Oceanic Technol.,* **20,** 99–116.

——, ——, J. L. Franklin, M. Goodberlet, J. Carswell, and A. S. Goldstein, 2007: Hurricane surface wind measurements from an operational stepped frequency microwave radiometer. *Mon. Wea. Rev.,* **135,** 3070–3085.

Willoughby, H. E., 1998: Tropical cyclone eye thermodynamics. *Mon. Wea. Rev.,* **126,** 3053–3067.

——, J. A. Clos, and M. G. Shoreibah, 1982: Concentric eye walls, secondary wind maxima, and the evolution of the hurricane vortex. *J. Atmos. Sci.,* **39,** 395–411.

Yuter, S. E., and R. A. Houze Jr., 1995: Three-dimensional kinematic and microphysical evolution of Florida cumulonimbus. Part II: Frequency distributions of vertical velocity, reflectivity, and differential reflectivity. *Mon. Wea. Rev.,* **123,** 1941–1963.

Zhang, J. A., R. F. Rogers, D. S. Nolan, and F. D. Marks Jr., 2011a: On the characteristic height scales of the hurricane boundary layer. *Mon. Wea. Rev.,* **139,** 2523–2535.

——, F. D. Marks Jr., M. T. Montgomery, and S. Lorsolo, 2011b: An estimation of turbulent characteristics in the low-level region of intense Hurricanes Allen (1980) and Hugo (1989). *Mon. Wea. Rev.,* **139,** 1447–1462.